

# AN ALL-SKY SAMPLE OF INTERMEDIATE-MASS STAR-FORMING REGIONS

Michael J. Lundquist<sup>1</sup>

Henry A. Kobulnicky<sup>1</sup>

Michael J. Alexander<sup>1,2</sup>

Charles R. Kerton<sup>3</sup>

Kim Arvidsson<sup>4</sup>

## ABSTRACT

We present an all-sky sample of 984 candidate intermediate-mass Galactic star-forming regions color-selected from the *Infrared Astronomical Satellite (IRAS)* Point Source Catalog and morphologically classify each object using mid-infrared *Wide-field Infrared Survey Explorer (WISE)* images. Of the 984 candidates, 616 are probable star-forming regions (62.6%), 128 are filamentary structures (13.0%), 39 are point-like objects of unknown nature (4.0%), and 201 are galaxies (20.4%). We conduct a study of four of these regions, IRAS 00259+5625, IRAS 00420+5530, IRAS 01080+5717, and IRAS 05380+2020, at Galactic latitudes  $|b| > 5^\circ$  using optical spectroscopy from the Wyoming Infrared Observatory along with near-infrared photometry from the Two-Micron All Sky Survey to investigate their stellar content. New optical spectra, color-magnitude diagrams, and color-color diagrams reveal their extinctions, spectrophotometric distances, and the presence of small stellar clusters containing  $20\text{--}78 M_\odot$  of stars. These low-mass diffuse star clusters contain  $\sim 65\text{--}250$  stars for a typical initial mass function, including one or more mid-B stars as their most massive constituents. Using infrared spectral energy distributions we identify young stellar objects near each region and assign probable masses and evolutionary stages to the protostars.

---

<sup>1</sup>Department of Physics and Astronomy, University of Wyoming, Laramie, WY 82071 USA

<sup>2</sup>Department of Physics, Lehigh University, 16 Memorial Drive East, Bethlehem, PA 18015 USA

<sup>3</sup>Department of Physics and Astronomy, Iowa State University, Ames, IA 50011 USA

<sup>4</sup>Trull School of Sciences & Mathematics, Schreiner University, 2100 Memorial Blvd., Kerrville, TX 78028 USA

The total infrared luminosity lies in the range 190 to 960  $L_{\odot}$ , consistent with the sum of the luminosities of the individually identified young stellar objects.

## 1. Introduction

It is well established that most stars form in groups or clusters (Larson 1982). Weidner & Kroupa (2006) suggested that an underlying physical relationship exists between the most massive star in an embedded cluster and the total stellar mass of the cluster. Low-mass stars tend to form in small, loose aggregates of 10–100 stars pc<sup>-3</sup> (Testi et al. 1999), while high-mass stars are associated with clusters that contain up to 1000 stars pc<sup>-3</sup> (Hillenbrand et al. 1995). Evidence suggests that there may be a turn-on mass for stellar clustering at the scale of intermediate-mass stars of 8–10  $M_{\odot}$  and that this onset may be sudden (Testi et al. 1997) or gradual (Testi et al. 1999). Hence, identifying and studying clusters having intermediate-mass stars as their most massive members may yield clues about the onset of cluster formation.

While it is reasonably well understood how isolated, low-mass stars form (McKee & Ostriker 2007), it may not be as simple as scaling this standard theory to explain high-mass star formation (Zinnecker & Yorke 2007). Scaling up low-mass star formation to higher masses ( $>10 M_{\odot}$ ) results in stars that begin to burn hydrogen while still accreting. The resulting radiation pressure should expel the accreting material preventing more massive stars from forming, yet stars much more massive do exist (Larson & Starrfield 1971; Zinnecker & Yorke 2007; Krumholz et al. 2009). At least two competing theories have been proposed to explain this paradox. In the competitive accretion model, stars within a common gravitational potential accrete from a distributed gas reservoir. The potential funnels gas down toward the cluster center, so the stars located closer to the center of the potential accrete at higher rates than isolated stars (Bonnell et al. 1997, 2001; Bonnell & Bate 2006). In the turbulent core accretion model, molecular clumps fragment into gaseous cores that subsequently collapse to make individual stars. As gas accretes onto the protostar, gravitational energy is released that heats up the surrounding gas. This increase in gas temperature raises the Jeans mass which suppresses fragmentation and results in fewer, but more massive, stars. This monolithic collapse would dictate a correlation of the clump mass with the stellar mass, as the mass of the core determines the mass reservoir available to form the star (McKee & Tan 2003; Krumholz et al. 2005; Krumholz & Bonnell 2007). These divergent theories have led to increased interest in studying star-forming regions that occupy the transition from the low- to high-mass regimes.

Arvidsson et al. (2010) defined and introduced a small sample of 70 intermediate-mass

star-forming regions (IM SFRs) — regions producing stars up to but not exceeding  $\sim 8 M_{\odot}$ . IM SFRs populate the continuum linking the low- and high-mass star-forming regimes where the onset of cluster formation may occur and the mechanisms that differentiate high-mass from low-mass star formation may become significant. IM SFRs are sites of star formation distinct from regions of high-mass star formation. They have typical luminosities of  $\sim 10^4 L_{\odot}$  and typical diameters of  $\sim 1$  pc, as judged from the sizes of the surrounding photodissociation regions (PDRs). They are typically associated with molecular clumps of mass  $\sim 10^3 M_{\odot}$ . The molecular material associated with IM SFRs typically has an order of magnitude lower peak mass column density and clump mass compared to ultra-compact HII regions which are examples of high-mass star formation (Arvidsson et al. 2010).

We have begun a program to study the stellar properties and the local environments surrounding IM SFRs and identify a larger more complete sample of IM SFRs. Our primary goal in this paper is to identify the stellar content and confirm the intermediate-mass nature of these candidate IM SFRs. In Section 2 we define an all-sky sample of IM SFRs and categorize them based on their mid-IR morphological appearance. In Section 3 we use the Two Micron All-Sky Survey (2MASS) Point Source Catalog (Cutri et al. 2003), new optical spectroscopy, and YSO SED fitting to investigate the stellar content of a sample of four IM SFRs. In Section 4 we present the results of our stellar content analysis, and we summarize key results in Section 5.

## 2. Sample Selection

Kerton (2002) used *Infrared Astronomical Satellite (IRAS)* mid-infrared fluxes and H I 21-cm emission maps to detect photodissociation regions (PDRs) associated with embedded intermediate-mass stars. These were used to define candidate IM SFRs using a set of color selection criteria that specifies cool dust and large polycyclic aromatic hydrocarbon (PAH) contribution:  $-0.18 < \log(F_{\nu}(25)/F_{\nu}(12)) < 0.4$ ,  $0.96 < \log(F_{\nu}(60)/F_{\nu}(25)) < 1.56$ , and  $0.29 < \log(F_{\nu}(100)/F_{\nu}(60)) < 0.69$ . For all candidate IM SFRs, the *IRAS* flux density quality flag was required to be either high ( $F_{\text{qual}} = 3$ ) or moderate ( $F_{\text{qual}} = 2$ ).

Arvidsson et al. (2010) adopted the Kerton (2002) criteria to define a sample totaling 984 candidate IM SFRs and used *Spitzer* Galactic Legacy Infrared MidPlane Survey Extraordinaire (GLIMPSE I) (Benjamin et al. 2003) and MIPSGAL I (Carey et al. 2005) legacy surveys to morphologically classify 70 inner-Galaxy targets that had complementary  $^{13}\text{CO}$  spectra from the Boston University Five College Radio Astronomy Observatory (BU-FCRAO) Galactic Ring Survey (GRS; Jackson et al. 2006). They classified the candidate objects into three groups based on their mid-IR morphologies: “blobs/shells,” “filamentary,”

and “star-like.” Arvidsson et al. (2010) found that the blobs/shells are star-forming regions characterized by circular or elliptical morphologies in the 8.0 and 24  $\mu\text{m}$  images. The filamentary objects appear to be small knots along larger filamentary structures including regions where filaments intersect. Star-like objects exhibit compact emission from one or more point sources in the mid-IR bands. The Arvidsson et al. (2010) pilot study classified 49 (70.0%) objects as blobs/shells, 11 (15.7%) objects as filamentary, and 10 (14.3%) as star-like.

Arvidsson et al. (2010) measured molecular column densities for 28 blobs/shells, of which 15 had distance determinations. All 15 blob/shells with distance determinations, and thus masses, lie below the 1 g  $\text{cm}^{-2}$  minimum mass column density threshold for high-mass star formation posited by Krumholz & McKee (2008). They found that these regions lack or have weak thermal radio continuum, limiting the most massive star(s) to early B or later, i.e., stars capable of exciting the PAHs, but not ionizing hydrogen. Arvidsson et al. (2010) also found typical luminosities of  $\sim 10^4 \text{ L}_\odot$ , where a luminosity of  $10^3\text{--}10^4$  corresponds roughly to a single  $\sim 4\text{--}10 \text{ M}_\odot$  young stellar object (Robitaille et al. 2006). On the basis of these properties they concluded that these regions host, at most, intermediate-mass stars, though the stellar content was not directly observed.

We used *Wide-field Infrared Survey Explorer* (*WISE*; Wright et al. 2010) 12 and 22  $\mu\text{m}$  images to extend the morphological classifications to the entire sample of 984 candidate IM SFRs. We introduce a new category, “galaxies”, to the “blobs/shells,” “filamentary,” and “star-like” scheme of Arvidsson et al. (2010). Figure 1 is a three-color rgb image (*WISE* 22  $\mu\text{m}$ , *WISE* 12  $\mu\text{m}$ , *WISE* 3.4  $\mu\text{m}$ ) that shows typical objects for each morphological category. The blobs/shells are characterized by extended emission at 12 and 22  $\mu\text{m}$ , including isolated blobs, shells, and also enhancements at the edges of pillars or bright-rimmed clouds. The filamentary objects appear to be long, narrow, low-surface-brightness wisps of emission at 12 and 22  $\mu\text{m}$ . The star-like objects appear as isolated point sources (occasionally multiple) in all *WISE* bands. The galaxies exhibit extended emission that appears circular or lenticular in all *WISE* bands, but they also have extended emission in near-infrared 2MASS and optical DSS images, rendering their morphology unmistakable. Of the 984 candidate IM SFRs, 616 (62.6%) are classified as blobs/shells, 128 (13.0%) are classified as filamentary, 39 (4.0%) are classified as star-like, and 201 (20.4%) are classified as galaxies. Table 1 lists the *IRAS* source name, coordinates, and morphological classification for all 984 objects in the sample. Figure 2 shows the distribution of these regions projected on the sky in Galactic coordinates. Red triangles correspond to blobs/shells, green diamonds to filamentary, blue stars to star-like, and grey squares to galaxies. Figure 2 illustrates that galaxies dominate the sample at high Galactic latitudes while blobs/shells, filamentary structures, and star-like objects are heavily concentrated toward the Galactic Plane. There is a conspicuous over-density of filamentary objects that constitutes nearly one-third of all filamentary objects, 41 of

the 128, around  $\ell = 80^\circ$  corresponding to the Cygnus-X region. This overdensity may be a result of the massive star content (Odenwald & Schwartz 1993) coupled with the relative proximity of the region at  $\sim 1.2\text{--}1.4$  kpc (Kobulnicky et al. 2013). There is also an overdensity of nine objects classified as blobs/shells around  $\ell = 280^\circ$ ,  $b = -32^\circ$ , at the location of the Large Magellanic Cloud. Another object classified with the blobs/shells (IRAS 00402+4120) is located in M31.

Taken together, the distribution of the morphological classes on the sky is consistent with the blobs/shells and filaments being star-forming regions (or affiliated with star-forming regions) in the Galactic Plane. The uniform distribution of galaxies is consistent with their classification as extra-Galactic sources. The nature of the star-like objects is not known. Some of these are likely to be very compact star-forming regions, perhaps akin to the Ultra-Compact Embedded Clusters (UCECs) identified by Alexander & Kobulnicky (2012). Some of these may be post- or pre- main sequence objects with circumstellar disks, such as IRAS 00487+5118 (#22 in Table 1) a Vega-type excess source (Dent et al. 2005). Higher resolution mid-IR imaging and/or infrared spectroscopy would help discern the nature of these sources.

Figure 3 plots the 984 candidate IMSFRs in a  $\log(f_\nu(25)/f_\nu(12))$  vs.  $\log(f_\nu(60)/f_\nu(25))$  *IRAS* color-color diagram. The box indicates the Kerton (2002) color selection domain, and the symbols denote candidate regions by morphological type as in Figure 2. The larger symbols with error bars indicate the mean color and error of the mean for each morphological type. The  $\log(f_\nu(60)/f_\nu(25))$  color is a measure of dust temperature while the  $\log(f_\nu(25)/f_\nu(12))$  color is sensitive to the PAH contribution. While the galaxies are more concentrated toward the higher dust temperatures at the left of the diagram, the mean colors of the blobs/shells, filamentary, and star-like objects are indistinguishable. The density of points drops markedly toward the right edge (low dust temp) and bottom edge (high PAH-to-dust ratio) of the plot, suggesting that a more generous color selection box would not yield significantly more objects. Given the combination of our color criteria and follow-up morphological classification, it is likely that our list of 984 candidate objects contains a reasonably complete sample of intermediate-mass star forming regions, at least to the limits imposed by *IRAS* sensitivity and beamsize ( $1.5' \times 4.7'$  at  $60\ \mu\text{m}$ ). The sample list could be expanded by a more generous color selection box toward higher dust temperatures, but this would lead to larger contamination by galaxies and require additional visual examination. Expanding the color selection toward smaller PAH-to-dust content would pick up additional star forming regions, but many of these would be increasingly dominated by massive, ionizing stars (e.g., see van der Veen & Habing 1988; Walker et al. 1989; Zhang et al. 2004).

### 3. A Pilot Survey of Stellar Content in Four Intermediate-Mass Star-Forming Regions

While Arvidsson et al. (2010) studied the gaseous content of a sample of inner-Galaxy IM SFRs, the stellar content of these regions remains unexplored. We have selected four outer-Galaxy intermediate-mass regions classified as blobs/shells and having four or more optically visible stars for an initial study of the stellar content of IM SFRs. The regions in this initial study are isolated and at high Galactic latitudes where there is expected to be less extinction and little confusion with other Galactic star forming regions. Table 2 lists the *IRAS* names, central positions, and *IRAS* fluxes of these sources. Figures 4 and 5 show three-color rgb images (*WISE* 22  $\mu\text{m}$ , 12  $\mu\text{m}$ , 3.4  $\mu\text{m}$ ) of the four IM SFRs. Cyan crosses mark the locations of optically visible stars selected for spectroscopic study (discussed in Section 3.2 below). White circles indicate 2–3.5' diameter regions used to search for possible stellar clusters using photometry from the Two Micron All Sky Survey (2MASS) Point Source Catalog (Cutri et al. 2003). Red circles indicate candidate YSOs. Black diamonds indicate maser sources, and white diamonds indicate sub-mm sources.

#### 3.1. Infrared Photometry

We used the 2MASS Point Source Catalog to generate  $JHK_S$  color-magnitude diagrams (CMDs) and color-color diagrams (CCDs) of each region. Figures 6 and 7 (top row) plot the raw  $K_S$  vs.  $J - K_S$  diagram for each region enclosed within the circles shown in Figures 4 and 5. As field stars can outnumber the associated main-sequence and pre-main sequence stars in a region, they must be removed statistically from the CMD to recover the likely cluster stars. We use the cluster cleaning tool of Alexander et al. (2013) which follows the prescription of Maia et al. (2010) to evaluate and remove the field star contamination. The middle row of panels in Figure 6 and 7 show the  $K_S$  vs.  $J - K_S$  diagrams for the field region. The field region is an annulus surrounding the cluster aperture that covers eight times the area of the cluster aperture. The field star estimation tool compares a target region to a field region using a 2MASS  $JHK_S$  3-dimensional color-color-magnitude diagrams (CCMD). After investigating different color and magnitude combinations for the CCMDs, we used the  $J$ ,  $J - H$ , and  $J - K_S$  magnitudes, as in Maia et al. (2010) for field subtraction. The lower row of panels in Figure 6 and 7 show the field-subtracted  $K_S$  vs.  $J - K_S$  cluster CMDs. The solid line is a Padova (Marigo et al. 2008; Girardi et al. 2010) zero-age main sequence that has been placed at the estimated distance and reddening (discussed in Section 4 below). The dotted, dashed, and dot-dashed lines indicate Siess et al. (2000) 0.5, 2.5, and 10.0 Myr pre-main-sequence isochrones respectively. Stars with optical spectra are indicated by pluses

and labeled by spectral type.

Figure 8 and 9 show the  $J - H$  vs.  $H - K_S$  CCDs cleaned in the same manner as Figure 6. The top row plots the raw  $J - H$  vs.  $H - K_S$  CCDs for each region enclosed within the circles shown in Figures 4 and 5. The middle row of panels plots  $J - H$  vs.  $H - K_S$  for the field region. The lower row of panels in Figure 8 and 9 show the field-subtracted  $J - H$  vs.  $H - K_S$  cluster CCDs. The solid line is a Padova (Marigo et al. 2008; Girardi et al. 2010) ZAMS that has been placed at the estimated reddening (discussed in Section 4 below). Stars having optical spectroscopy are indicated by pluses and labeled by spectral type.

We interpret these CMDs and CCDs in Section 4 to look for compact stellar populations of similar reddening and distance.

### 3.2. Optical Spectroscopy

We used the CMDs and CCDs described above in conjunction with optical catalogs to select sources within the four candidate IM SFRs having bright  $K_S$ -band magnitudes and  $V \lesssim 16$ . This  $K_S$ -band magnitude criterion includes the stars that are likely to be the most luminous and, therefore, the most massive cluster members. We obtained optical spectra for eighteen sources using the LongSlit spectrograph on the Wyoming Infrared Observatory (WIRO) 2.3 m telescope in 2011 December and 2012 September. Each object lies within the central 1–2' of the four candidate IM SFRs. The data for nine of the eighteen objects were obtained with a 600  $1 \text{ mm}^{-1}$  grating giving a spectral coverage of 4000–7000 Å at a typical reciprocal dispersion of  $\sim 1.5 \text{ \AA pixel}^{-1}$  across the chip. The remaining nine spectroscopic targets were observed with a 2000  $1 \text{ mm}^{-1}$  grating giving a spectral coverage of 5400–6800 Å at a typical reciprocal dispersion of  $\sim 0.72 \text{ \AA pixel}^{-1}$ . The typical signal to noise ratio at 5500 Å was greater than 40 with several stars exceeding 200. The data were reduced in the standard manner using dome lamp flat-fielding, bias frames, and CuAr comparision lamp spectra for wavelength calibration to a typical precision of 0.015 Å rms for the 2000  $1 \text{ mm}^{-1}$  grating and 0.05 Å rms for 600  $1 \text{ mm}^{-1}$ .

### 3.3. Spectral Classification

Extinction by dust along the line of sight produces low signal-to-noise in the typical temperature diagnostic He I  $\lambda 4471 \text{ \AA}$  and Mg II  $\lambda 4481 \text{ \AA}$  lines, making classifications difficult for B- and early A-type stars. In our spectra the available lines that are useful for spectral classification of these stars are the He II  $\lambda 5411 \text{ \AA}$ , He I  $\lambda 5876 \text{ \AA}$ , and H $\alpha$   $\lambda 6563 \text{ \AA}$  lines. The

absence of the He II  $\lambda 5411$  Å line in all of our spectra limits the spectral type to B0.5 or later. The absence of the He I  $\lambda 5876$  Å line in some of the targets limits the spectral type to later than about A0. The EW of the H $\alpha$  line is at a maximum at a spectral type of about A1, but is double-valued, decreasing in strength for stars both earlier and later.

Spectral classification was done by comparision with the spectral atlas of Jacoby et al. (1984) and by comparison to the spectral indices of Hernández et al. (2004) and Kobulnicky et al. (2012). For B-stars this included comparisions of the equivalent widths of H $\alpha$  and He I  $\lambda 5876$  Å. For A- and F-stars this included comparisions of the equivalent width of H $\alpha$ . For G-stars this included comparisions of the equivalent width of H $\alpha$  and the Mg I triplet at  $\lambda\lambda 5167, 5172, 5183$  Å. For K-stars this included comparisions of the equivalent width of H $\alpha$  and visual comparisions with the MgH band at  $\lambda 5000$ – $5200$  Å. Spectral classifications of B-, A- and F-type stars are typically certain to  $\pm 1$  spectral sub-type for a typical signal to noise ratio of 40 using this method. He I and H $\alpha$  lack the sensitivity to differentiate B0.5–B3 stars, so the two stars that appear to fall in this range have been classified as B2. Owing to interstellar extinction and limited wavelength coverage, no stars have the combination of good signal-to-noise in the blue part of the optical range needed for luminosity classification; in the absence of constraining data, we assume that all stars are luminosity class V, but we caution that this may not always be the case.

Table 3 lists the relevant parameters for determining the spectral types and spectrophotometric distances for each star. Column 1 lists the *IRAS* region name and the corresponding alphabetic identifier in Figures 4 and 5 for each star with optical spectra. Column 2 lists the 2MASS ID. Columns 3–5 list the  $J$ -,  $H$ -, and  $K_S$ - band magnitudes given by the 2MASS Point Source Catalog. Columns 6–9 list the equivalent widths and equivalent width uncertainties for H $\alpha$  and He I, the primary spectral lines used to determine spectral types. Column 10 lists the estimated spectral type. Column 11 shows the extinction determined from the 2MASS magnitudes and the spectral type including upper and lower limits assuming an uncertainty of  $\pm 1$  sub-type for B-, A-, and F- type stars and  $\pm 3$  sub-types for G-type and later stars. Column 12,  $D_{spec}$ , is the spectrophotometric distance determined from the 2MASS magnitudes and the spectral type, including upper and lower limits, where the upper/lower limits result from the random uncertainty in spectral type and the second *upper-only* limit accounts for systematic uncertainty resulting from the unknown binarity status of each star; if any of these stars are close binaries with equal-luminosity companions (common among massive stars; Kiminki & Kobulnicky 2012), the distances could be underestimated by as much as  $\sqrt{2}$ . Column 13,  $D_{lit}$ , lists distances found in literature for each region. Estimates of the distance to each region were done by using 2MASS  $H - K_S$  color excesses to derive  $A_V$  and  $A_K$  using a Cardelli et al. (1989) extinction curve. A distance modulus was calculated with  $A_K$ , the 2MASS  $K_S$ -band magnitude, and the intrinsic  $K_S$ -band magnitude

from a Padova zero age main-sequence (ZAMS) isochrone, assuming the observed stars are dwarfs (luminosity class V). The uncertainties on the distance estimates are dominated by the uncertainties on our spectral classifications and the (unknown) binary status.

### 3.4. Young Stellar Objects

The young stellar objects (YSOs) near each region were identified by generating spectral energy distributions (SEDs) using 2MASS  $JHK_S$  near-IR and *WISE* 3.4, 4.5, 12, and 22  $\mu\text{m}$  mid-IR data with source cross-band matching done from the *WISE* Point Source Catalog which includes 2MASS. These sources were fit using the SED fitting tool of Robitaille et al. (2007) in a similar manner to Alexander et al. (2013).

All *WISE* point sources within  $10'$  of the IM SFR were selected for fitting. We required a minimum of three photometric data points per target and removed objects that did not meet this criterion. We first fit sources to Kurucz (1993) stellar models where we allowed the extinction parameter to vary from  $A_V = 0$  to 40 magnitudes. Sources with  $\chi^2/n_{data} \leq 2$  were deemed to be well fit by a reddened stellar photosphere and removed. To remove sources with bad fits due to high mid-IR sky backgrounds, the remaining sources were visually inspected at *WISE* bands W3 and W4 and removed if they did not appear to be point sources. The SED fitting tool was then used to fit the remaining sources to a grid of 200,000 YSO model SEDs (Robitaille et al. 2006). Table 4 lists the input parameters for this fit. Column 1 indicates which IRAS target field contains the YSO. Column 2 lists the assigned YSO ID. Column 3 gives the *WISE* ID. Columns 4–6 indicate the 2MASS PSC magnitudes. Columns 7–10 list the *WISE* PSC magnitudes. We chose model aperture sizes of  $3''$  for 2MASS,  $6''$  for *WISE* bands W1, W2, and W3, and  $12''$  for *WISE* band W4 for all regions, while the extinction parameter varied from  $A_V = 0$  to 35 magnitudes for all regions. We allowed the distance parameter to vary from 1.5–2.5 kpc for IRAS 00259+5625, 2.0–2.5 kpc for IRAS 00420+5530 (best estimate maser distance), 1.0–2.0 kpc for IRAS 01082+5717, and 0.7–1.5 kpc for IRAS 05380+2020. We selected models where the fits were limited to  $(\chi^2 - \chi^2_{best})/n_{data} < 2$  and used a weighted average to estimate YSO properties in the manner of Alexander et al. (2013).

Table 5 compiles the results of the YSO fitting. This table lists the number of models well fit to each YSO SED and the  $\chi^2/n_{data}$  as a measure of the goodness of fit. It also lists best fit and average values for the extinction, stellar mass, disk mass, and disk accretion rate, in addition to the range of stellar mass fit by the models and the total YSO luminosity. These parameters were used to determine the stage of the YSO. (Robitaille et al. 2006) assigns stage 0/I for heavily embedded sources with envelope accretion rates  $\dot{M}/M_* > 10^{-6}$

$\text{yr}^{-1}$ . Stage II YSOs have  $\dot{M}/M_* < 10^{-6} \text{ yr}^{-1}$  and  $M_{\text{disk}}/M_* > 10^{-6}$ . They have little or no mass left in the envelope, but are young enough to still have a protostellar disk. Stage III YSOs  $\dot{M}/M_* < 10^{-6} \text{ yr}^{-1}$  and  $M_{\text{disk}}/M_* < 10^{-6}$ . They have little or no mass left in either an envelope or a protostellar disk. Sources with fits that do not have a total weight (probability) greater than 0.67 for any single stage are assigned as ambiguous (amb).

## 4. The Stellar Content of IM SFRs

### 4.1. IRAS 00259+5625

IRAS 00259+5625 was classified as an IM SFR in the Bok globule CB3 by Codella & Bachiller (1999) due to its IR bolometric luminosity of  $930 L_\odot$  (Launhardt & Henning 1997). Launhardt & Henning (1997) found a kinematic distance of 2.5 kpc assuming that IRAS 00259+5625 was associated with the near side of the Perseus arm. Yun & Clemens (1994) obtained  $^{12}\text{CO}$  velocity distance of 2.1 kpc using the Clemens (1985) rotation curve. There is a compact submillimeter source likely consisting of an aggregate of multiple Class 0 sources  $15''$  west and  $6''$  south of the IRAS 00259+5625 source position (Huard et al. 2000) indicated by the white diamond in the left panel of 4. The black diamond in the left panel of 4 indicates an  $\text{H}_2\text{O}$  maser also present in the region (Scappini et al. 1991).

Figure 10 shows our optical spectra of the five stellar targets. Black solid lines denote our spectra, while the dotted lines show the best comparison spectra from the Jacoby et al. (1984) spectral atlas. Star A has a weak He I  $\lambda 5876 \text{ \AA}$  absorption feature ( $EW=0.29 \pm 0.13 \text{ \AA}$ ) and a strong  $\text{H}\alpha$  absorption line ( $EW=7.99 \pm 0.57 \text{ \AA}$ ), indicative of a mid-B star (B7). Star B has a spectrum with strong  $\text{H}\alpha$  absorption ( $EW=14.95 \pm 0.17 \text{ \AA}$ ) indicative of an early A star (A1). Star C has strong, narrow  $\text{H}\alpha$  absorption ( $EW=4.53 \pm 0.19 \text{ \AA}$ ) indicative of an mid-F star (F6). Star D has weak, narrow  $\text{H}\alpha$  absorption and the presence of the Mg I triplet at  $\lambda\lambda 5167, 5172, 5183 \text{ \AA}$  indicative of an early G star (G0). Star E has a weaker, narrow  $\text{H}\alpha$  absorption and an increasing presence of the Mg I triplet at  $\lambda\lambda 5167, 5172, 5183 \text{ \AA}$  indicative of a late-G star (G9). We used the spectrum of Star B and its 2MASS magnitudes and colors to derive a spectrophotometric distance of  $1.65^{+0.04+0.68}_{-0.08}$  kpc with an extinction of  $A_V = 1.03^{+0.04}_{-0.03}$  mag for the region.

IRAS 00259+5625 contains four candidate YSOs in the vicinity of the IM SFR. These include three intermediate-mass YSOs (Y1, Y2, and Y3) at  $4.0$ ,  $2.8$ , and  $3.0 M_\odot$  and one lower-mass YSOs (Y4) at  $0.8 M_\odot$ . Of the three intermediate-mass YSOs, two are Stage II YSOs (Y2 and Y3), while the Y1 fit is ambiguous. The lower-mass YSO, Y4, is Stage I. The total luminosity contribution of these YSOs is  $2.4 \times 10^2 L_\odot$ . Using the Sanders & Mirabel

(1996) definition for infrared luminosity, we use the *IRAS* fluxes to derive an infrared luminosity of  $3.1 \times 10^2 L_{\odot}$  for the region, which is consistent with a total luminosity from the most massive YSOs identified and tabulated in Table 5.

The cleaned CMD of IRAS 00259+5625 in the left panel of Figure 6 is rather sparse, showing just a few sources near the nominal main sequence at a distance of 1.65 kpc and reddening of  $A_V = 1.03$  mag. Star B, found to be an early A star from our optical spectroscopy, is labeled and lies near the nominal A0V star (lower X) along the main sequence. Star A ( $\sim$ B7) is not drawn because the 2MASS Catalog lists only upper limits for its J and H photometry as the source is detected, but not resolved from a nearby companion, in these bands. Stars C and D (mid- to late-F) lie just to the right of the main sequence along the 10 Myr isochrone near where it joins the main sequence. These appear slightly too bright to be mid-F stars at the adopted cluster distance and reddening; they may be foreground objects at  $d \simeq 0.6$  kpc (see Table 3), or they could be binary/multiple systems having magnitudes brighter than those of single stars of the equivalent type. It is unlikely that they are overluminous pre-main-sequence objects because our optical spectra do not show the H $\alpha$  emission signatures of active accretion. Star E, found to be a late-G type, lies well to the upper right of the main sequence (brighter and redder), consistent with it possibly being a field giant. A group of about eight stars lie along the 2.5 and 10 Myr isochrones, most of them near  $J - K_S = 1.2$ , at the locations where late-stage pre-main-sequence stars would be expected. Another sequence of about eight stars stretch redward from pre-main-sequence tracks, consistent with them being either enshrouded pre-main-sequence stars or more reddened background objects. Of the four YSOs in this region, three lie within the marked cluster aperture (Y1, Y3, and Y4), but only Y4 appears on Figure 6 near  $K = 13.67$ ,  $J - K_S = 2.6$ . The other two lie off the plot because of their extreme colors ( $J - K_S \sim 4.6$ ). The color-color diagram for IRAS 00259+5625 (Figure 8) reveals a loose group of stars near  $H - K_S = 0.4$ ,  $J - H = 1.0$ , with a few stretching along the reddening vector to more extreme colors. This grouping of stars may consist of moderately reddened ( $A_V \sim 4$ ) intermediate-mass stars, lightly reddened low-mass stars, or some combination thereof. Taken together, the cleaned CMD, CCD, and the spectra of IRAS 00259+5625 are consistent with a poor cluster of pre-main-sequence stars in the vicinity of the mid-B, early A, and late-F stars that appear to be the most massive constituents of this region. The limited depth of the 2MASS photometry precludes a more definitive characterization of the possible stellar cluster in IRAS 00259+5625, though using the Weidner et al. (2013) most massive star – cluster mass relation, we can estimate a total cluster mass of  $\sim 20 M_{\odot}$  in  $\sim 65$  stars above  $0.1 M_{\odot}$  after integrating a typical Kroupa (2001) IMF.

#### 4.2. IRAS 00420+5530

Kumar et al. (2006) investigated the IRAS 00420+5530 region and found it to contain a  $380 M_{\odot}$  cluster. Molinari et al. (2002) used millimeter data to determine that this region had a bolometric luminosity of  $L = 12,400 L_{\odot}$  at a kinematic distance of 5.0 kpc. Based on its radio free-free flux, they also determined that a  $\sim 3000 L_{\odot}$  B2 ZAMS star was present. Zhang et al. (2005) found a kinematic distance of 7.72 kpc. Moellenbrock et al. (2009) obtained a distance of 2.17 kpc via trigonometric parallax of an H<sub>2</sub>O maser. The maser is indicated by the black diamond in the right panel of Figure 4. Koenig et al. (2012) noted a small cluster of YSOs associated with this region and considered it to be distinct from the nearby massive star-forming region NGC 281, for which Sato et al. (2008) obtained an H<sub>2</sub>O maser trigonometric parallax distance of 2.82 kpc. Rygl et al. (2010) suggested that both IRAS 00420+5530 and NGC 281 may be on the edge of an expanding superbubble.

Figure 11 shows spectra of the four stars that were obtained revealing two intermediate-mass stars. Star A has a spectrum with a weak He I  $\lambda 5876 \text{ \AA}$  absorption feature ( $EW=0.19 \pm 0.02 \text{ \AA}$ ) and a strong H $\alpha$  emission feature ( $EW=-8.663 \pm 0.02 \text{ \AA}$ ). Spectral classification using the He I line results in a B8e star; however, the He I EW may be a lower limit if there is a nebular emission in that line, therefore, the temperature class could be earlier than B8. Furthermore, this wavelength region lacks the luminosity diagnostics to distinguish a classical Be star from a B supergiant. As a result, the spectrophotometric distance for star A was not calculated. Star B has a spectrum with strong He I  $\lambda 5876 \text{ \AA}$  absorption ( $EW=0.73 \pm 0.12 \text{ \AA}$ ) and H $\alpha$  absorption ( $EW=4.491 \pm 0.27 \text{ \AA}$ ) that appears to indicate an early B star (B2). Star C has strong, narrow H $\alpha$  absorption ( $EW=6.339 \pm 0.13 \text{ \AA}$ ) indicative of an early F star (F2). Star D has a strong, narrow H $\alpha$  absorption ( $EW=4.00 \pm 0.07 \text{ \AA}$ ) indicative of a late-F star (F9). We used the spectrum of Star B and its 2MASS colors to derive a spectrophotometric distance of  $1.14^{+0.34+0.47}_{-0.25}$  kpc at an extinction of  $A_V = 6.33^{+0.17}_{-0.17}$  mag for this region. This distance is not consistent with the maser parallax distance measurement of 2.17 kpc, though the agreement is better than with the kinematic distance measurements of  $>5$  kpc. A portion of this discrepancy can be reconciled if Star B is in a binary system with a companion of nearly equal luminosity.

IRAS 00420+5530 contains nine candidate YSOs in the vicinity of the IM SFR. These include eight intermediate-mass YSOs and one lower-mass YSO. Of the eight intermediate-mass YSOs, two are Stage I (Y7 and Y12), three are Stage II (Y5, Y10, and Y13), one is Stage III (Y11), and two fits are ambiguous (Y6 lies between Stage I and II and Y9 lies between Stage II and III). The lower-mass YSO, Y8, is Stage I. Y6 apparently coincides spatially with Star C. The spectrum obtained of Star C is consistent with an early F temperature class and shows no indication of accretion. The SED model fits, however, are consistent with a  $5.1 M_{\odot}$

YSO. This may indicate that a foreground F star (estimated distance 0.46 kpc) is projected in front of the IR emission from a intermediate-massive YSO with the IM SFR estimated to lie at 2.2 kpc. In that case, the flux contribution from the YSO and the foreground star would be ambiguous in the 2MASS bands increasing the uncertainty in the YSO fit. The calculated spectrophotometric distance and extinction listed in Table 3 is almost certainly in error because of this possible blend. The total luminosity contribution of these YSOs is  $9.6 \times 10^2 L_{\odot}$ . Using the Sanders & Mirabel (1996) definition for infrared luminosity, we use the *IRAS* fluxes to derive an infrared luminosity of  $8.8 \times 10^2 L_{\odot}$  at 1.14 kpc or  $3.2 \times 10^3 L_{\odot}$  at 2.17 kpc. The total YSO luminosity is consistent with the closer spectro-photometric distance, but if the cluster is at the maser parallax distance would suggest that there are more intermediate-mass YSOs contributing to the infrared luminosity that have not been accounted for.

The cleaned color-magnitude diagram of IRAS 00420+5530 is rather rich, showing a distinct grouping of stars near the nominal main sequence at a distance of 1.14 kpc and reddening of  $A_V = 6.33$  mag. Star A lies to the left of the main sequence and is possibly a foreground classical Be star. Star B, found to be an early B star from our optical spectroscopy, is labeled and lies near the nominal B0V star (upper X) along the main sequence. Stars C and D (early to late-F) lie to the left of the main sequence. These appear too bright to be mid-F stars at the adopted cluster distance and reddening; they are likely foreground objects at  $d \simeq 0.26$  kpc and  $d \simeq 0.71$  (see Table 3). A group of about 25 stars lies near or below the nominal main sequence, most of them between  $J - K_S = 1.2 - 1.7$ . Another sequence of about eight stars stretch redward from pre-main-sequence tracks, consistent with them being either enshrouded pre-main-sequence stars or more reddened background objects. Two of the nine YSOs identified in the IRAS 00420+5530 field lie within the marked cluster aperture (Y6 and Y12). Star C (Stage II/III;  $\equiv$ Y6?) appears on Figure 6 near  $K_S = 9.98$ ,  $J - K_S \simeq 0.6$  and is likely a foreground object along the line of sight toward the YSO, as discussed above. Y12 (Stage I/II;  $5.3 M_{\odot}$ ) appears on Figure 6 near  $K_S = 9.95$ ,  $J - K_S \simeq 3.1$  where a young, enshrouded pre-main-sequence star would be expected. The color-color diagram for IRAS 00420+5530 (Figure 8) reveals that the rich grouping of stars from the color-magnitude diagram has a large spread in color from  $H - K_S = 0.1$  to  $H - K_S = 0.8$ . There are a few stars stretching along the reddening vector to more extreme colors, including Y12. Several of these stars appear to have  $H - K_S$  colors redder than would be expected for main-sequence objects at higher reddening. This suggests that these are possible pre-main-sequence stars with k-band excesses. The nature of the stars that lie to the left of the main sequence is less clear. The unusually blue  $H - K_S$  colors may be the result of reflection nebulosity or poor 2MASS photometry as these stars have typical uncertainties of  $\sim 0.2$  mag in  $J$ -,  $H$ -, and  $K_S$ -bands. Taken together, the cleaned CMD, CCD and the spectra of IRAS 00420+5530 are

consistent with a cluster of pre-main-sequence stars in the vicinity of the early B star that appear to be the most massive constituent of this region. Using the Weidner et al. (2013) most massive star – cluster mass relation, we estimate a total cluster mass of  $\sim 78 M_{\odot}$  in  $\sim 250$  stars above  $0.1 M_{\odot}$  after integrating a typical Kroupa (2001) IMF.

### 4.3. IRAS 01082+5717

IRAS 01082+5717 has largely been unexplored in literature. It was identified as a site of diffuse *IRAS* emission with a radius of  $9'$  by Fich & Terebey (1996) in a survey of *IRAS* 60  $\mu\text{m}$  images.

Figure 12 shows the spectra of the four stellar targets revealing three intermediate-mass stars. Star A has a spectrum with a strong He I  $\lambda 5876 \text{ \AA}$  absorption feature ( $EW=0.53\pm0.01 \text{ \AA}$ ) and strong H $\alpha$  absorption ( $EW=7.14\pm0.52 \text{ \AA}$ ), indicative of a mid-B star (B4). Star B shows a weak He I  $\lambda 5876 \text{ \AA}$  absorption feature ( $EW=0.15\pm0.02 \text{ \AA}$ ) and an H $\alpha$  absorption feature ( $EW=7.40\pm0.06 \text{ \AA}$ ) indicating a late-B star (B8). Star C exhibits a weak He I  $\lambda 5876 \text{ \AA}$  absorption feature ( $EW=0.15\pm0.03 \text{ \AA}$ ) and an H $\alpha$  absorption feature ( $EW=8.76\pm0.14 \text{ \AA}$ ) indicating a late-B star (B8). Star D has a strong, narrow H $\alpha$  absorption feature ( $EW=3.798\pm0.07 \text{ \AA}$ ) indicative of an early G star (G0). The separation between Star B and Star C is  $\sim 2''$  leading to blending in the 2MASS images. Unfiltered guide camera images taken at the time as the spectroscopic observations indicate that Stars B and C are roughly the same visual magnitude. The 2MASS catalog photometry for Star B, which includes the flux contribution from Star C, is included in the CMD and CCD for reference, and in Table 3. We used the spectrum of Star A and its 2MASS photometry to derive a spectrophotometric distance of  $1.84^{+0.26+0.76}_{-0.23} \text{ kpc}$  at an extinction of  $A_V = 1.22^{+0.09}_{-0.11} \text{ mag}$  for this region.

IRAS 01082+5717 contains five YSOs, all of intermediate mass and all Stage II (Y14, Y15, Y16, Y17, and Y18) in the vicinity of the IM SFR. Y16–Y18 all lie outside the nominal cluster aperture shown in Figure 5, but they are still in the field of IRAS 01082+5717. Y15 corresponds to Star A. The spectrum of Star A presents as a mid-B star ( $\sim 5 M_{\odot}$ ) at an  $A_V$  of 1.22 mag and shows no indication of accretion. This agrees with the average SED model fit of a  $3.1 M_{\odot}$  YSO at an average  $A_V$  of 1.12 mag. The mean extinctions for the five YSOs vary from 0.86 – 9.6 mag., but this could be the result of differential extinction within the SFR coupled with the limited precision of the SED fitting technique. The total luminosity contribution of these YSOs is  $2.8 \times 10^2 L_{\odot}$ . Using the Sanders & Mirabel (1996) definition for infrared luminosity, we use the *IRAS* fluxes to derive an infrared luminosity of  $1.9 \times 10^2 L_{\odot}$  for the region.

The cleaned color-magnitude diagram of IRAS 01082+5717 is rather sparse, showing just a few sources near the nominal main sequence at a distance of 1.84 kpc and reddening of  $A_V = 1.22$  mag. Star A, found to be a mid-B star from our optical spectroscopy, is labeled and lies between the nominal B0V and A0V loci (upper and lower X's) along the main sequence. Star B (late-B) lies above its expected location on the main sequence. This is likely owing to confusion with Star C (late-B), which was not drawn owing to its lack of photometry in the 2MASS catalog. Star D (early G) lies just to the right of and above the main sequence consistent with it possibly being a foreground dwarf or background giant. Accordingly, we do not compute a spectrophotometric distance for this star. A group of about seven stars lie along the 2.5 Myr isochrone at locations where pre-main-sequence stars would be expected. Another sequence of about five stars lie along the main-sequence track. There is also a group of about five stars that stretch redward from pre-main-sequence tracks, consistent with them being either enshrouded pre-main-sequence stars or more reddened background objects. Two of the five YSOs identified in this field lie within the marked cluster aperture (Y14 and Y15). Y14 appears on Figure 7 near  $K = 13.28$ ,  $J - K_S \simeq 1.5$ . Y15 (Star A) lies along the main sequence at the adopted distance and reddening based upon its spectral type. The color-color diagram (Figure 9) reveals a sparse group of stars near  $H - K_S = 0.3$ ,  $J - H = 0.8$ , with a few stretching along the reddening vector to more extreme colors. Three of these stars appear to have k-band excesses which suggest that they may be pre-main-sequence stars. Taken together, the cleaned CMD, CCD, and the spectra are consistent with the region hosting a poor cluster of pre-main-sequence stars in the vicinity of the mid-B and late-B stars that appear to be the most massive constituents. The limited depth of the 2MASS photometry precludes a more definitive characterization of the possible stellar cluster in IRAS 01082+5717, though using the Weidner et al. (2013) most massive star – cluster mass relation, we can estimate a total cluster mass of  $\sim 37 M_\odot$  in  $\sim 120$  stars above  $0.1 M_\odot$  after integrating a typical Kroupa (2001) IMF.

#### 4.4. IRAS 05380+2020

IRAS 05380+2020 is a star-forming region included in an H I survey by Lu et al. (1990) who found a galaxy with a redshift of  $6735 \text{ km s}^{-1}$  at this position. Takata et al. (1994) argued that the infrared luminosity is very high and not compatible with the H I profile of a galaxy at such a distance, indicating that there is likely a galaxy behind this Galactic infrared source.

Figure 13 shows the five spectra that were obtained for IRAS 05380+2020, revealing three intermediate-mass stars. Star A has a strong He I  $\lambda 5876 \text{ \AA}$  absorption feature

( $EW=0.71\pm0.33$  Å) and H $\alpha$  absorption ( $EW=5.61\pm0.13$  Å). This spectrum is indicative of an early B star (B2). Star B has weak He I  $\lambda 5876$  Å absorption ( $EW=0.19\pm0.06$  Å) and an H $\alpha$  absorption feature ( $EW=6.63\pm0.20$  Å) indicating a late-B (B8) star. Star C has a strong H $\alpha$  absorption feature ( $EW=14.40\pm0.11$  Å) indicating an early A star (A1). Star D has a narrow H $\alpha$  absorption ( $EW=2.94\pm0.24$  Å) indicative of a mid-G (G4) star. Star E has a very narrow H $\alpha$  absorption feature ( $EW=1.06\pm0.07$  Å) and a strong Fe I  $\lambda 6495$  Å absorption feature indicative of an early K (K0) star. We used the spectrum of Star A and its 2MASS photometry to derive a spectrophotometric distance of  $1.34^{+0.40+0.55}_{-0.30}$  kpc at an extinction of  $A_V = 2.74^{+0.17}_{-0.17}$  mag for this region.

IRAS 05380+2020 contains two candidate YSOs in the vicinity of the IM SFR. Of these, Y19 is of intermediate mass and Y20 is of lower mass. Y19 is Stage I and Y20 is ambiguously fit by the models (I/II). Y19 is poorly fit as a result of a  $\sim 5$  magnitude increase from the  $K_S$  band to the *WISE* W1 band. This may be owing to variability of the source in the  $\sim 12$  years between the 2MASS and *WISE* observations. The total luminosity contribution of these YSOs is  $8.7 \times 10^1$  L $_{\odot}$ . Using the Sanders & Mirabel (1996) definition for infrared luminosity, we use the *IRAS* fluxes to derive an infrared luminosity of  $2.5 \times 10^2$  L $_{\odot}$ .

The cleaned color-magnitude diagram of IRAS 05380+2020 is rather rich, showing a distinct grouping of stars near the nominal main sequence at a distance of 1.34 kpc and reddening of  $A_V = 2.74$  mag. Star A, found to be an early B star from our optical spectroscopy, is labeled and lies near the nominal B0V locus (upper X) along the main sequence. Star B, found to be a late-B star, is labeled and lies between the nominal B0V and A0V loci along the main sequence. Star C lies to the left of the main sequence and above the nominal A0V locus. This appears too bright to be an early A star at the adopted cluster distance and reddening; this is likely a foreground object at  $d \simeq 0.78$  kpc and correspondingly lower reddening,  $A_V=0.61$  mag (see Table 3). A group of about 28 stars scatters about the nominal 2.5 Myr isochrone, most of them between  $J - K_S=1.2 - 1.6$ . Another sequence of about six stars stretches redward from the pre-main-sequence tracks, consistent with them being either enshrouded pre-main-sequence stars or more reddened background objects. One of the two YSOs (Y19) lies within the marked cluster aperture. Y19 is located on Figure 7 near  $K=15.18$ ,  $J - K_S=1.75$  where a young, enshrouded pre-main-sequence star would be expected. The color-color diagram for IRAS 05380+2020 (Figure 9) reveals that the rich grouping of stars from the color-magnitude diagram has a small spread in  $J - H$  color, but a large spread in  $H - K_S$  color from 0.2 to 0.7. There is also a grouping along the main sequence and several stars stretching along the reddening vector to more extreme colors. Several stars appear to have k-band excesses suggesting possible pre-main-sequence stars. Taken together, cleaned CMD, CCD, and the spectra are consistent with a cluster of pre-

main-sequence stars in the vicinity of the early and mid-B stars that appear to be the most massive constituents of this region. Using the Weidner et al. (2013) most massive star – cluster mass relation, we estimate a total cluster mass of  $\sim 78 M_{\odot}$  in  $\sim 250$  stars above  $0.1 M_{\odot}$  after integrating a typical Kroupa (2001) IMF.

#### 4.5. Initial Mass Function Modeling

Given that low- and intermediate- mass clusters suffer from stochastic effects when populating the upper end of the initial mass function, we utilize the stellar cluster simulation software MASSCLEAN (Popescu & Hanson 2009) to model the clusters in our pilot study. MASSCLEAN allows for stochastic fluctuations in the simulations. We compute the mass distribution using a Kroupa-Salpeter initial mass function (Kroupa 2002; Salpeter 1955) with an upper mass limit of  $150 M_{\odot}$ . We randomly generate 1000 clusters for a range of total cluster masses from  $3-1000 M_{\odot}$  in  $1 M_{\odot}$  bins and tabulate the fraction that reproduce the upper end of the mass function observed in our clusters. Figure 14 shows the fraction of simulated clusters within each mass bin producing a cluster with the most massive star  $2 M_{\odot} \leq M_{\text{max}} \leq 8 M_{\odot}$  (solid bold line) and the most massive star  $4 M_{\odot} \leq M_{\text{max}} \leq 10 M_{\odot}$  (dotted bold line). We also explored requiring the cluster to have exactly two stars in the mass range  $2 M_{\odot} \leq M \leq 8 M_{\odot}$  including the most massive star (solid light line) and requiring the cluster to have exactly two stars in the mass range  $4 M_{\odot} \leq M \leq 10 M_{\odot}$  including the most massive star (dotted, light line). The lines in Figure 14 have been smoothed to 3 solar mass bins to reduce scatter. This simulation demonstrates that it is likely that clusters forming only two intermediate mass stars have a total mass between  $20$  and  $80 M_{\odot}$ , consistent with masses estimated from the Weidner et al. (2013) most massive star – cluster mass relation. While we cannot completely rule out that these are fairly massive clusters that have happened not to form a massive star, it is highly improbable that clusters with intermediate-mass stars as their most massive constituents have a total mass greater than  $150 M_{\odot}$ . While it is common for a massive cluster to produce a massive star and eject it via few-body interactions to become a runaway OB star, it is highly improbable to dynamically eject the most massive star from a cluster with  $< 316 M_{\odot}$  (Oh & Kroupa 2012).

#### 5. Summary and Conclusions

In this paper we morphologically classify an all-sky sample of 984 candidate IM SFRs using *WISE* mid-IR images. The objects in this all-sky sample were selected from the *IRAS* Point Source Catalog using colors that indicate large PAH contribution and cool dust found

in IM SFRs. We determined that 616 (62.6%) are classified as “blobs/shells,” 128 (13.0%) are classified as “filamentary,” 39 (4.0%) are classified as “star-like” objects, and 201 (20.4%) are classified as “galaxies.” We find that the blobs/shells, filamentary, and star-like objects are concentrated in the Galactic Plane, while galaxies appear to be uniformly distributed throughout the sky.

We conducted a pilot study of four Galactic IM SFRs that are classified as blobs/shells using optical spectroscopy and near-IR photometry. Optical spectroscopy of four–five stars per region demonstrates that each contains, within its projected boundaries, two or more intermediate-mass stars. Eight of the eighteen spectroscopically classified stars are B-type and two are A-type with no stars more massive than  $\sim$ B2 ( $8 M_{\odot}$ ) found. Near-IR color-magnitude diagrams using 2MASS data indicate that these stars are the most massive & luminous constituents, suggesting that there may be an upper limit to the mass of stars in IM SFRs of  $\sim$ B2. SEDs of candidate YSOs in each region also indicate that they are continuing to produce intermediate- and lower-mass stars, but not massive stars. These findings support the idea that the *IRAS* color-selection of (Kerton 2002; Arvidsson et al. 2010) does indeed select regions producing intermediate-mass stars and that these regions can be distinguished from high-mass SFRs using *IRAS* mid-IR colors.

Cleaned 2MASS color-magnitude diagrams reveal a strong excess of stars along the pre-main-sequence isochrones in IRAS 00420+5530 and IRAS 05380+2020 and a less obvious excess in IRAS 00259+5625 and IRAS 01082+5717, indicating the presence of small clusters associated with the spectroscopically identified IM stars. The former two regions (IRAS 00420+5530 and IRAS 05380+2020) that have the strongest evidence for stellar clusters also the earliest stars as their most massive members ( $\sim$ B2), while the latter two clusters (IRAS 00259+5625 and IRAS01082+5717) host somewhat later spectral types (B7 and B4, respectively). Thus, the most massive stars appear to be associated with richer and more massive stellar clusters. While the current small sample size precludes a definitive statement, this correlation is consistent with the idea that there may be a turn-on point for cluster formation at the cloud masses and stellar masses associated with the formation of mid-B spectral types as the most massive constituent.

Acknowledgement: We would like to acknowledge the support of Carlos A. Vargas Alvarez, Anirban Bhattacharjee, Michael DiPompeo, and Jiajun Chen for their assistance in obtaining spectroscopy data. This work was supported by NASA through grants NAS2-97001 from the Stratospheric Observatory for Infrared Astronomy and ADAP NNX10AD55G. We thank James Weger and Jerry Bucher for their work in maintaining the Wyoming Infrared Observatory as an excellent astronomical facility. We would also like to thank the anonymous referee for his/her comments and suggestions, helping to improve this manuscript.

## REFERENCES

- Alexander, M. J. & Kobulnicky, H. A. 2012, ApJ, 755, L30
- Alexander, M. J., Kobulnicky, H. A., Kerton, C. R., & Arvidsson, K. 2013, ApJ, 770, 1
- Arvidsson, K., Kerton, C. R., Alexander, M. J., Kobulnicky, H. A., & Uzpen, B. 2010, AJ, 140, 462
- Benjamin, R. A., Churchwell, E., Babler, B. L., Bania, T. M., Clemens, D. P., Cohen, M., Dickey, J. M., Indebetouw, R., Jackson, J. M., Kobulnicky, H. A., Lazarian, A., Marston, A. P., Mathis, J. S., Meade, M. R., Seager, S., Stolovy, S. R., Watson, C., Whitney, B. A., Wolff, M. J., & Wolfire, M. G. 2003, PASP, 115, 953
- Bonnell, I. A. & Bate, M. R. 2006, MNRAS, 370, 488
- Bonnell, I. A., Bate, M. R., Clarke, C. J., & Pringle, J. E. 1997, MNRAS, 285, 201
- . 2001, MNRAS, 323, 785
- Cardelli, J. A., Clayton, G. C., & Mathis, J. S. 1989, ApJ, 345, 245
- Carey, S. J., Noriega-Crespo, A., Price, S. D., Padgett, D. L., Kraemer, K. E., Indebetouw, R., Mizuno, D. R., Ali, B., Berriman, G. B., Boulanger, F., Cutri, R. M., Ingalls, J. G., Kuchar, T. A., Latter, W. B., Marleau, F. R., Miville-Deschenes, M. A., Molinari, S., Rebull, L. M., & Testi, L. 2005, in Bulletin of the American Astronomical Society, Vol. 37, American Astronomical Society Meeting Abstracts, 1252
- Clemens, D. P. 1985, ApJ, 295, 422
- Clemens, D. P. & Barvainis, R. 1988, ApJS, 68, 257
- Codella, C. & Bachiller, R. 1999, A&A, 350, 659
- Cutri, R. M., Skrutskie, M. F., van Dyk, S., Beichman, C. A., Carpenter, J. M., Chester, T., Cambresy, L., Evans, T., Fowler, J., Gizis, J., Howard, E., Huchra, J., Jarrett, T., Kopan, E. L., Kirkpatrick, J. D., Light, R. M., Marsh, K. A., McCallon, H., Schneider, S., Stiening, R., Sykes, M., Weinberg, M., Wheaton, W. A., Wheelock, S., & Zacarias, N. 2003, 2MASS All Sky Catalog of point sources.
- Dent, W. R. F., Greaves, J. S., & Coulson, I. M. 2005, MNRAS, 359, 663
- Fich, M. & Terebey, S. 1996, ApJ, 472, 624

- Girardi, L., Williams, B. F., Gilbert, K. M., Rosenfield, P., Dalcanton, J. J., Marigo, P., Boyer, M. L., Dolphin, A., Weisz, D. R., Melbourne, J., Olsen, K. A. G., Seth, A. C., & Skillman, E. 2010, *ApJ*, 724, 1030
- Hernández, J., Calvet, N., Briceño, C., Hartmann, L., & Berlind, P. 2004, *AJ*, 127, 1682
- Hillenbrand, L. A., Meyer, M. R., Strom, S. E., & Skrutskie, M. F. 1995, *AJ*, 109, 280
- Huard, T. L., Weintraub, D. A., & Sandell, G. 2000, *A&A*, 362, 635
- Jackson, J. M., Rathborne, J. M., Shah, R. Y., Simon, R., Bania, T. M., Clemens, D. P., Chambers, E. T., Johnson, A. M., Dormody, M., Lavoie, R., & Heyer, M. H. 2006, *ApJS*, 163, 145
- Jacoby, G. H., Hunter, D. A., & Christian, C. A. 1984, *ApJS*, 56, 257
- Kerton, C. R. 2002, *AJ*, 124, 3449
- Kiminki, D. C. & Kobulnicky, H. A. 2012, *ApJ*, 751, 4
- Kobulnicky, H. A., Alexander, M. J., Lundquist, M. J., Long, G. R., Smullen, R., Bhattacharjee, A., & Vargas Alvarez, C. 2013, in American Astronomical Society Meeting Abstracts, Vol. 221, American Astronomical Society Meeting Abstracts, 142.02
- Kobulnicky, H. A., Lundquist, M. J., Bhattacharjee, A., & Kerton, C. R. 2012, *AJ*, 143, 71
- Koenig, X. P., Leisawitz, D. T., Benford, D. J., Rebull, L. M., Padgett, D. L., & Assef, R. J. 2012, *ApJ*, 744, 130
- Kroupa, P. 2001, *MNRAS*, 322, 231
- . 2002, *Science*, 295, 82
- Krumholz, M. R. & Bonnell, I. A. 2007, ArXiv e-prints
- Krumholz, M. R., Klein, R. I., McKee, C. F., Offner, S. S. R., & Cunningham, A. J. 2009, *Science*, 323, 754
- Krumholz, M. R. & McKee, C. F. 2008, *Nature*, 451, 1082
- Krumholz, M. R., McKee, C. F., & Klein, R. I. 2005, *Nature*, 438, 332
- Kumar, M. S. N., Keto, E., & Clerkin, E. 2006, *A&A*, 449, 1033
- Kurucz, R. L. 1993, SYNTHE spectrum synthesis programs and line data

- Larson, R. B. 1982, MNRAS, 200, 159
- Larson, R. B. & Starrfield, S. 1971, A&A, 13, 190
- Launhardt, R. & Henning, T. 1997, A&A, 326, 329
- Lu, N. Y., Dow, M. W., Houck, J. R., Salpeter, E. E., & Lewis, B. M. 1990, ApJ, 357, 388
- Lynds, B. T. 1965, ApJS, 12, 163
- Maia, F. F. S., Corradi, W. J. B., & Santos, Jr., J. F. C. 2010, MNRAS, 407, 1875
- Marigo, P., Girardi, L., Bressan, A., Groenewegen, M. A. T., Silva, L., & Granato, G. L. 2008, A&A, 482, 883
- McKee, C. F. & Ostriker, E. C. 2007, ARA&A, 45, 565
- McKee, C. F. & Tan, J. C. 2003, ApJ, 585, 850
- Moellenbroek, G. A., Claussen, M. J., & Goss, W. M. 2009, ApJ, 694, 192
- Molinari, S., Brand, J., Cesaroni, R., & Palla, F. 1996, A&A, 308, 573
- Molinari, S., Testi, L., Rodríguez, L. F., & Zhang, Q. 2002, ApJ, 570, 758
- Odenwald, S. F. & Schwartz, P. R. 1993, ApJ, 405, 706
- Oh, S. & Kroupa, P. 2012, MNRAS, 424, 65
- Popescu, B. & Hanson, M. M. 2009, AJ, 138, 1724
- Robitaille, T. P., Whitney, B. A., Indebetouw, R., & Wood, K. 2007, ApJS, 169, 328
- Robitaille, T. P., Whitney, B. A., Indebetouw, R., Wood, K., & Denzmore, P. 2006, ApJS, 167, 256
- Rygl, K. L. J., Brunthaler, A., Reid, M. J., Menten, K. M., van Langevelde, H. J., & Xu, Y. 2010, A&A, 511, A2
- Salpeter, E. E. 1955, ApJ, 121, 161
- Sanders, D. B. & Mirabel, I. F. 1996, ARA&A, 34, 749

- Sato, M., Hirota, T., Honma, M., Kobayashi, H., Sasao, T., Bushimata, T., Choi, Y. K., Imai, H., Iwadate, K., Jike, T., Kameno, S., Kameya, O., Kamohara, R., Kan-Ya, Y., Kawaguchi, N., Kim, M. K., Kuji, S., Kurayama, T., Manabe, S., Matsui, M., Matsumoto, N., Miyaji, T., Nagayama, T., Nakagawa, A., Nakamura, K., Oh, C. S., Omodaka, T., Oyama, T., Sakai, S., Sato, K., Shibata, K. M., Tamura, Y., & Yamashita, K. 2008, PASJ, 60, 975
- Scappini, F., Caselli, P., & Palumbo, G. G. C. 1991, MNRAS, 249, 763
- Siess, L., Dufour, E., & Forestini, M. 2000, A&A, 358, 593
- Takata, T., Yamada, T., Saito, M., Chamaraux, P., & Kazes, I. 1994, A&AS, 104, 529
- Testi, L., Palla, F., & Natta, A. 1999, A&A, 342, 515
- Testi, L., Palla, F., Prusti, T., Natta, A., & Maltagliati, S. 1997, A&A, 320, 159
- van der Veen, W. E. C. J. & Habing, H. J. 1988, A&A, 194, 125
- Walker, H. J., Volk, K., Wainscoat, R. J., Schwartz, D. E., & Cohen, M. 1989, AJ, 98, 2163
- Weidner, C. & Kroupa, P. 2006, MNRAS, 365, 1333
- Weidner, C., Kroupa, P., & Pflamm-Altenburg, J. 2013, MNRAS, 434, 84
- Wright, E. L., Eisenhardt, P. R. M., Mainzer, A. K., Ressler, M. E., Cutri, R. M., Jarrett, T., Kirkpatrick, J. D., Padgett, D., McMillan, R. S., Skrutskie, M., Stanford, S. A., Cohen, M., Walker, R. G., Mather, J. C., Leisawitz, D., Gautier, III, T. N., McLean, I., Benford, D., Lonsdale, C. J., Blain, A., Mendez, B., Irace, W. R., Duval, V., Liu, F., Royer, D., Heinrichsen, I., Howard, J., Shannon, M., Kendall, M., Walsh, A. L., Larsen, M., Cardon, J. G., Schick, S., Schwalm, M., Abid, M., Fabinsky, B., Naes, L., & Tsai, C.-W. 2010, AJ, 140, 1868
- Yun, J. L. & Clemens, D. P. 1994, ApJS, 92, 145
- Zhang, P., Chen, P. S., & He, J. H. 2004, New A, 9, 509
- Zhang, Q., Hunter, T. R., Brand, J., Sridharan, T. K., Cesaroni, R., Molinari, S., Wang, J., & Kramer, M. 2005, ApJ, 625, 864
- Zinnecker, H. & Yorke, H. W. 2007, ARA&A, 45, 481

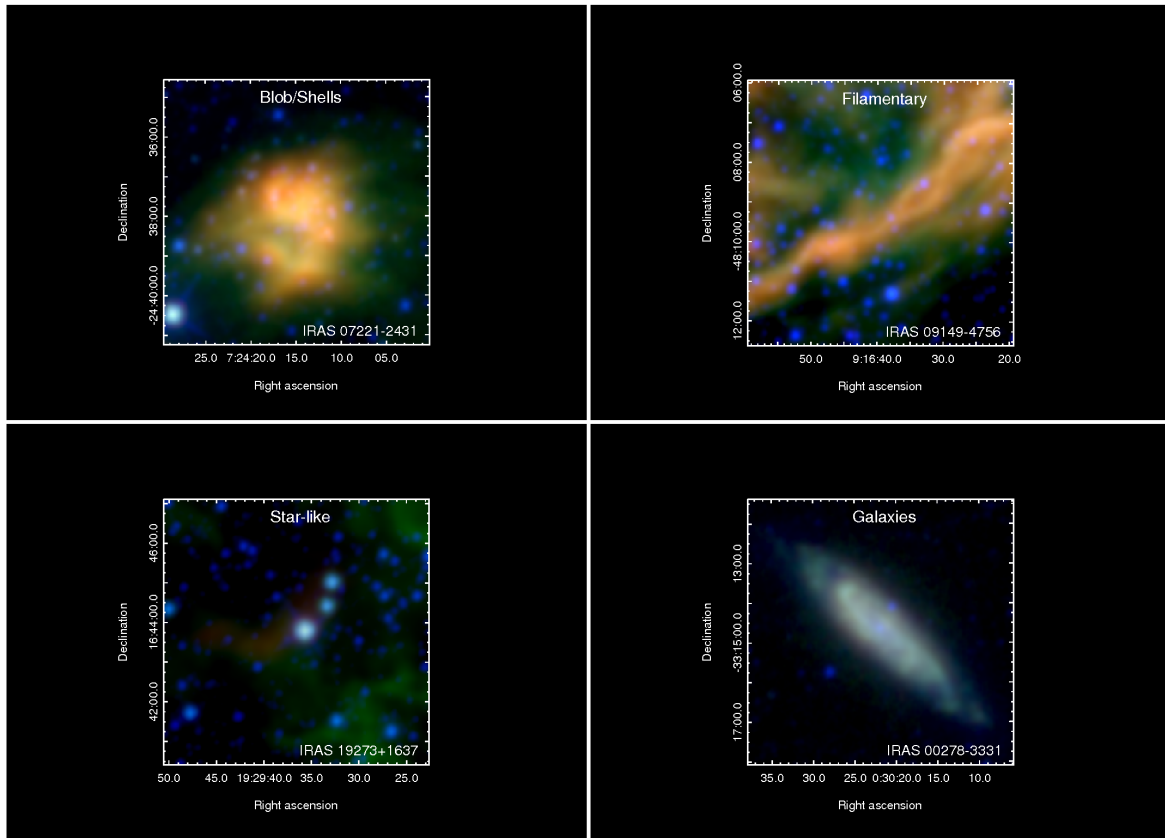


Fig. 1.— A three-color rgb image (*WISE* 22  $\mu\text{m}$ , 12  $\mu\text{m}$ , 3.4  $\mu\text{m}$ ) showing a typical example of objects that fulfill the *IRAS* color selection criteria for each morphological type: blobs/shells, filamentary, star-like, and galaxies.

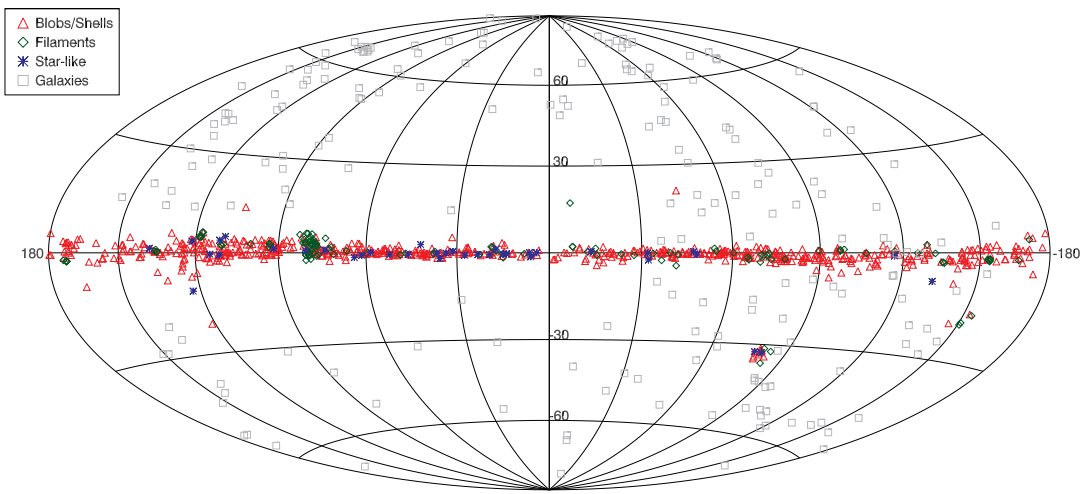


Fig. 2.— Aitoff projection in Galactic coordinates showing the spatial distribution of 984 candidate IM SFRs. The candidate IMSFRs are color-coded by morphological classification. Red triangles correspond to blobs/shells, green diamonds to filamentary objects, blue stars to star-like objects, and grey squares to galaxies. The blobs/shells, filamentary objects, and star-like objects are concentrated in the Galactic Plane with a small grouping in the Magellanic Clouds. (A color version of this figure is available in the online journal.)

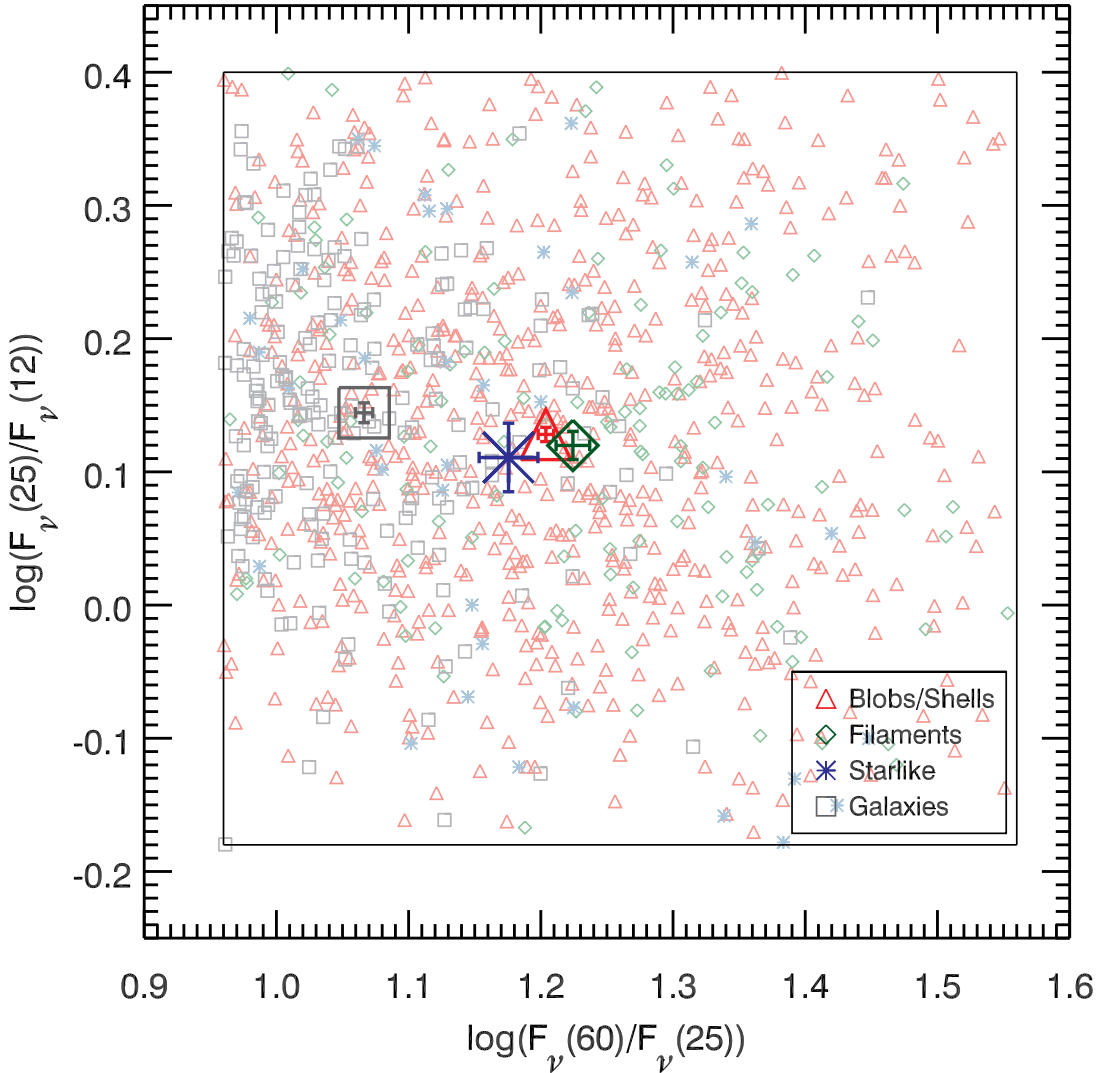


Fig. 3.— *IRAS* color-color diagram of the 984 candidate IM SFRs. The box indicates the boundaries of the *IRAS* color selection for the sample. Red triangles correspond to blobs/shells, green diamonds to filamentary objects, blue stars to star-like objects, and grey squares to galaxies. The larger, darker colored symbols, represent the average colors for each morphological type with error bars indicating the error of the mean. (A color version of this figure is available in the online journal.)

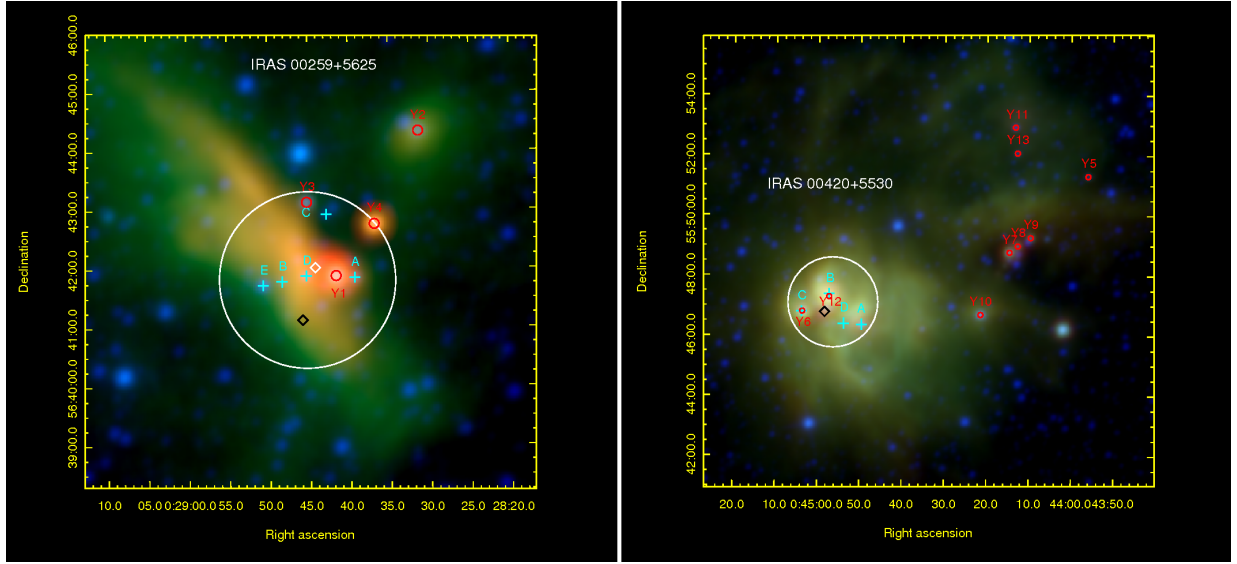


Fig. 4.— Three-color rgb image (*WISE* 22  $\mu\text{m}$ , 12  $\mu\text{m}$ , 3.4  $\mu\text{m}$ ) of IRAS 00259+5625 (left) and IRAS 00420+5530 (right). Cyan crosses indicate individual stars selected for optical spectroscopy, and white circles indicate the regions used to search for possible stellar clusters. White diamonds mark the positions of known sub-mm sources and black diamonds mark the positions of known masers.

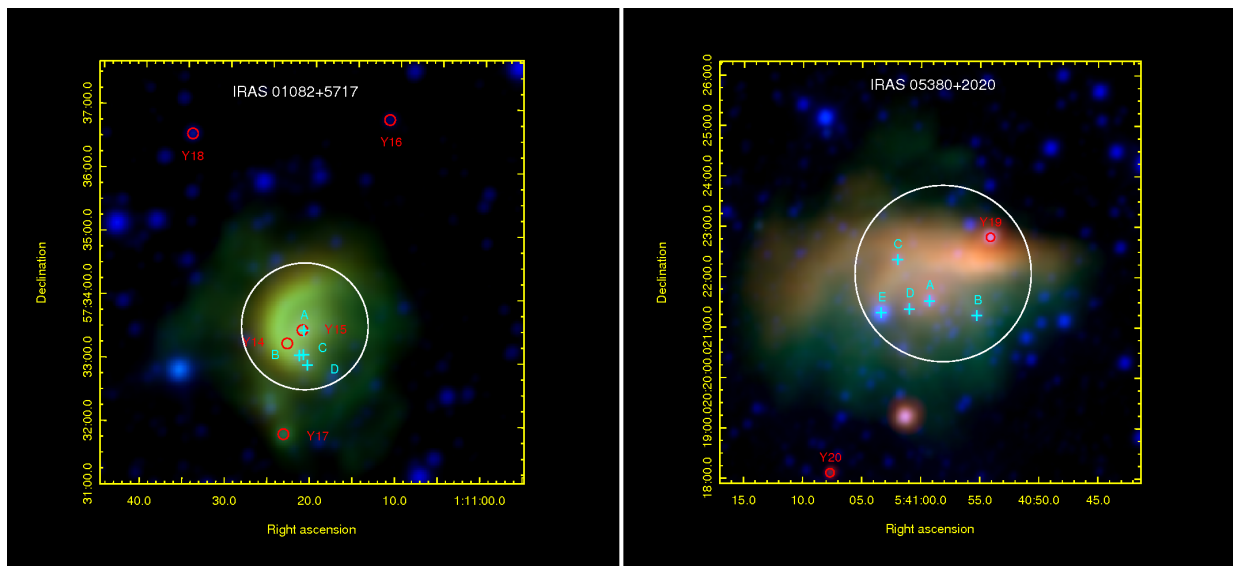


Fig. 5.— As Figure 4 for IRAS 01082+5717 (left) and IRAS 05380+2020 (right).

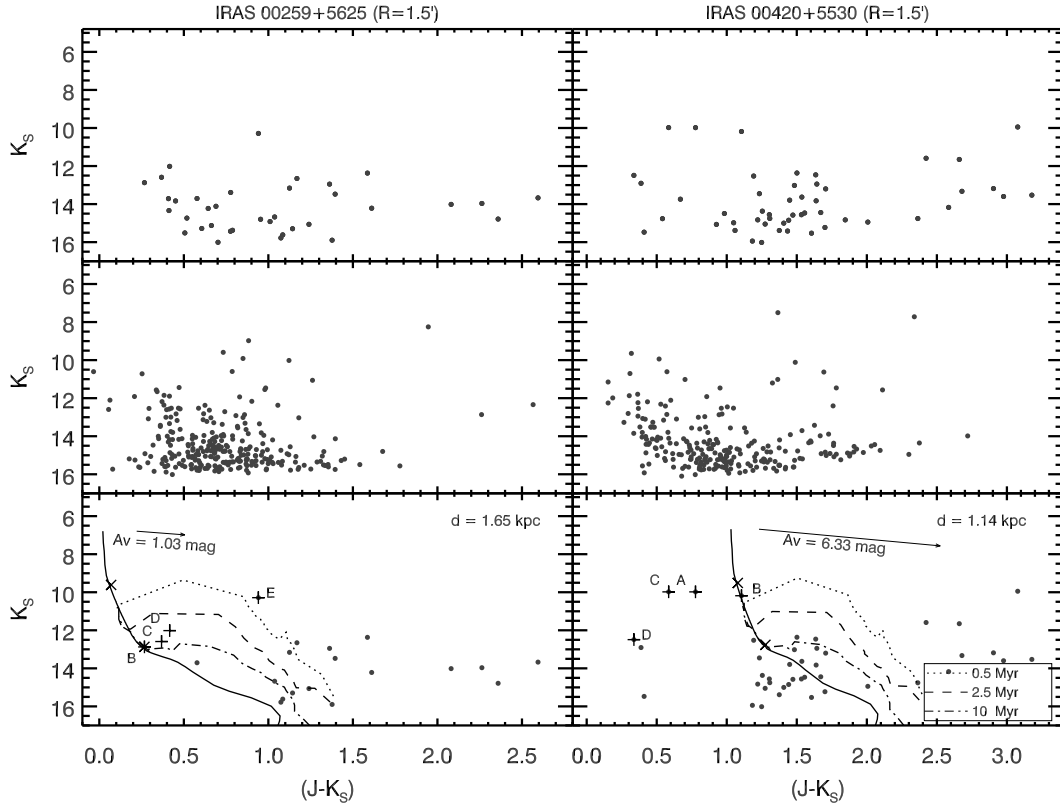


Fig. 6.— CMDs of IRAS 00259+5625 (left column) and IRAS 00420+5530 (right column) for the defined cluster region (top row), comparison field annulus (middle row), and the cleaned cluster region (bottom row). The lower panel shows a reddened Padova ZAMS isochrone (solid curve) with upper and lower X's indicating B0V and A0V locations, respectively. The cleaned cluster also shows reddened Siess 0.5 Myr (dotted line), 2.5 Myr (dashed curve), and 10 Myr (dotted-dashed curve) pre-main-sequence tracks. Pluses indicate stars selected for spectroscopy. The adopted distance and extinction are given in the lower panels. Arrows indicate the direction and magnitude of interstellar reddening, as labeled.

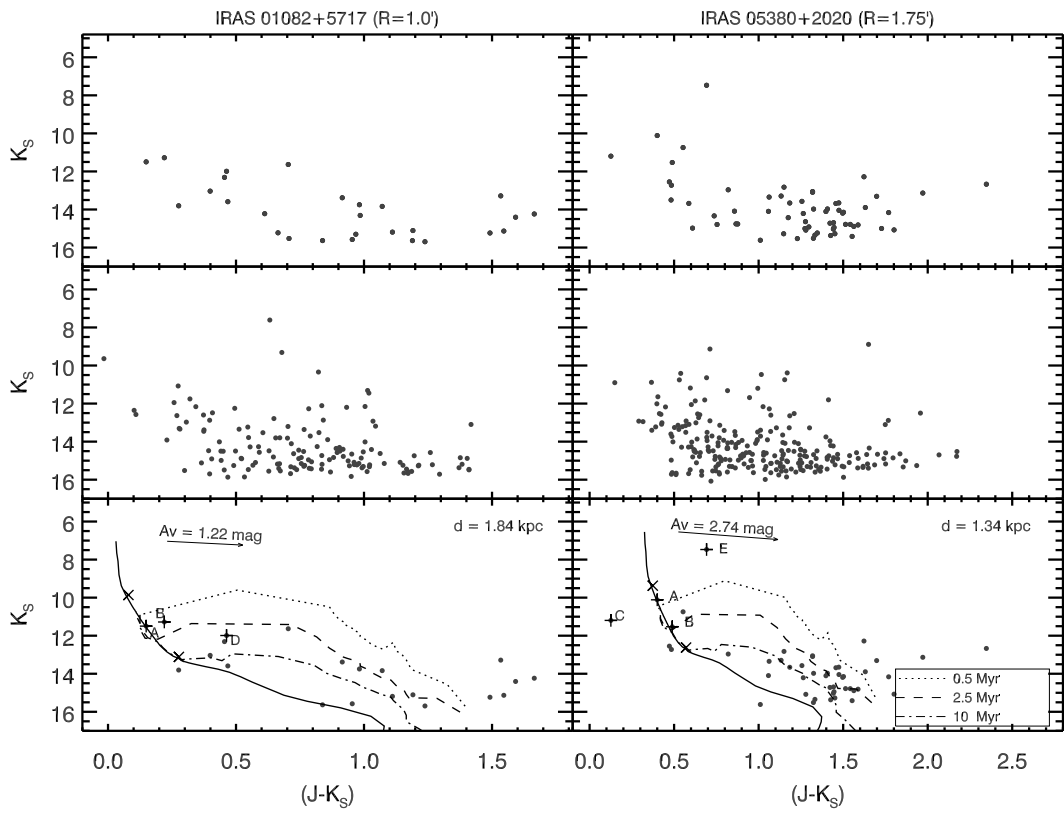


Fig. 7.— CMDs, as in Figure 6, for IRAS 01082+5717 (left column) and IRAS 05380+2020 (right column).

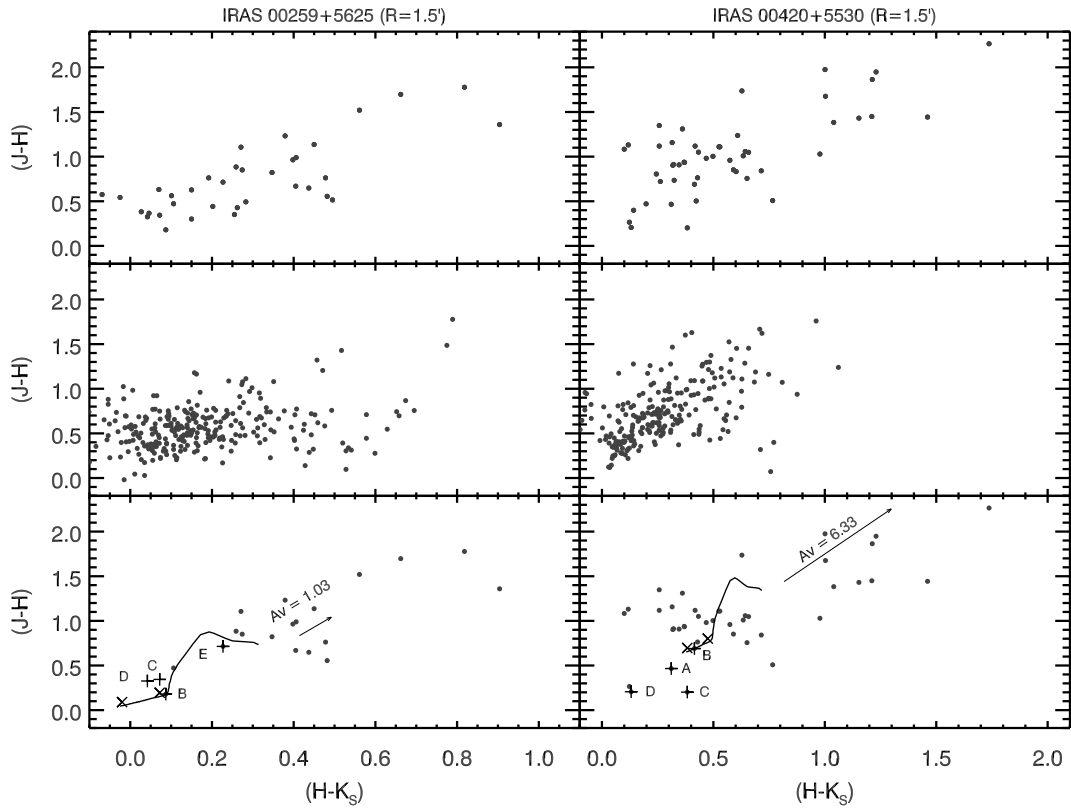


Fig. 8.— CCDs of IRAS 00259+5625 (left column) and IRAS 00420+5530 (right column) for the defined cluster region (top row), comparison field annulus (middle row), and the cleaned cluster region (bottom row). The solid curve in the lower panel shows a Padova ZAMS isochrone with upper and lower X's indicating the locations of B0V and A0V stars, respectively. Pluses indicate stars selected for spectroscopy. The extinction is given for each cleaned cluster, and arrows indicate the direction of the reddening vectors.

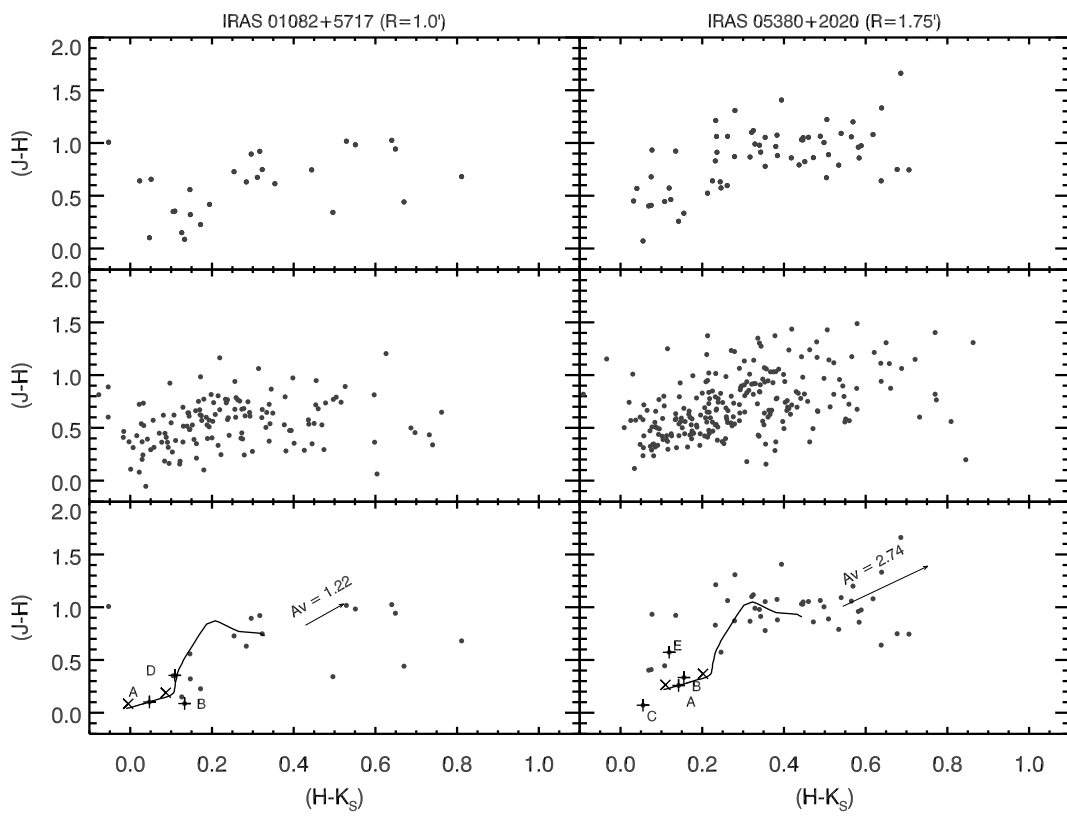


Fig. 9.— CCDs, as in Figure 8, for IRAS 01082+5717 (left column) and IRAS 05380+2020 (right column).

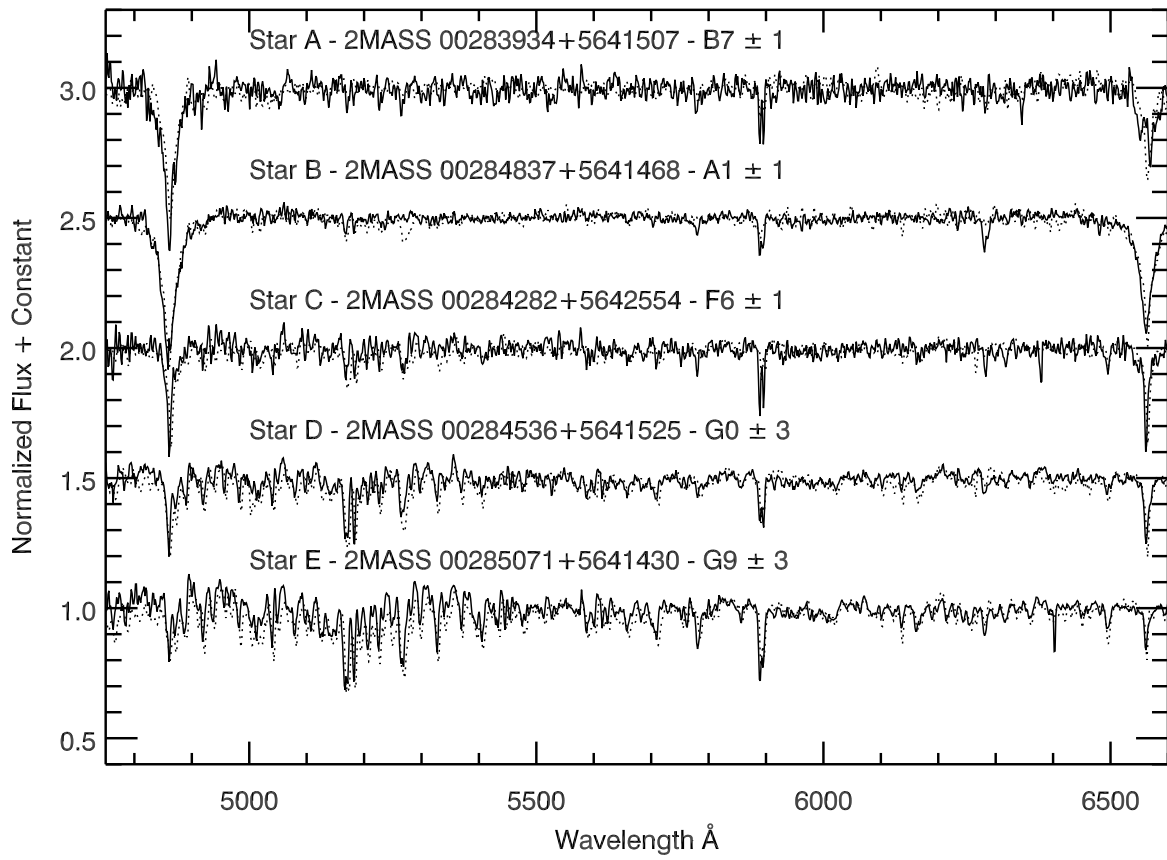


Fig. 10.— Continuum-normalized spectra (solid black lines) of the five stars selected for optical spectroscopy from IRAS 00259+5625. The spectra are overplotted with red dotted lines of comparable spectral type from the Jacoby et al. (1984) spectral atlas.

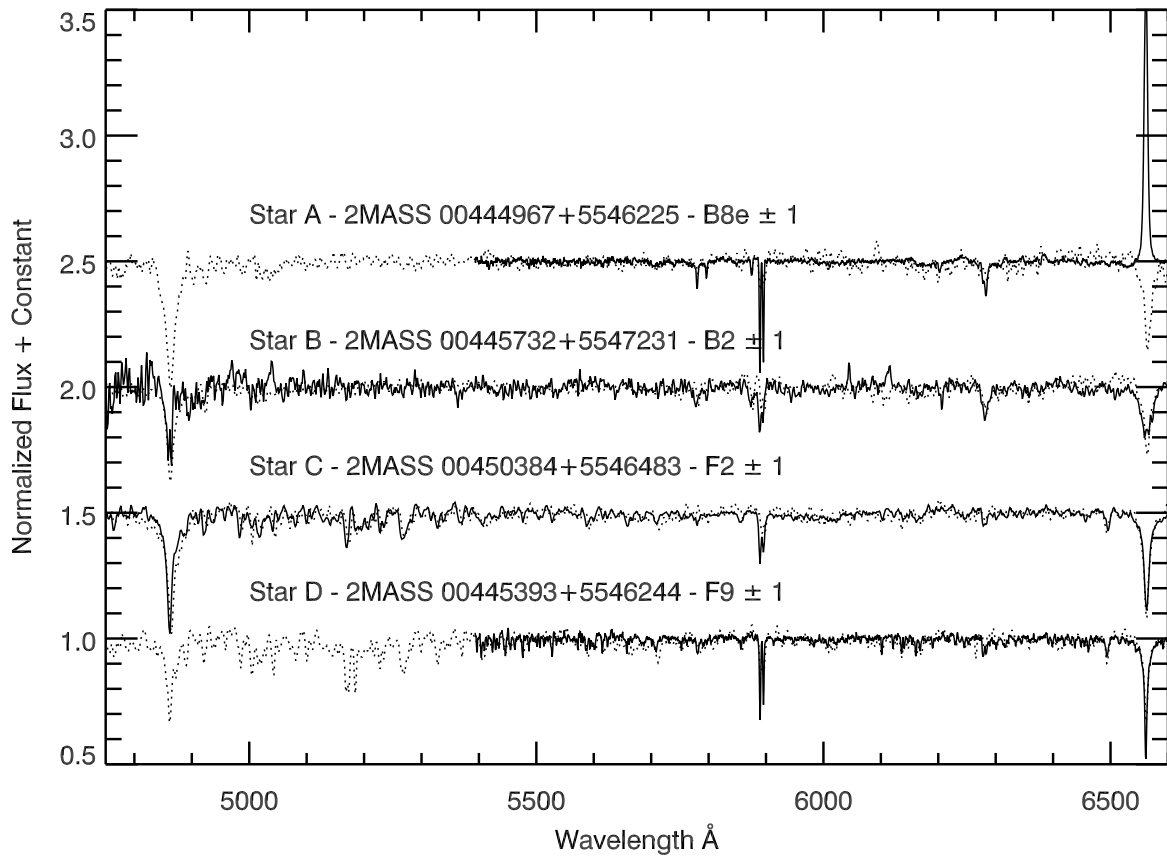


Fig. 11.— Continuum-normalized spectra (solid black lines) of the five stars selected for optical spectroscopy from IRAS 00420+5530. The spectra are overplotted with red dotted lines of comparable spectral type from the Jacoby et al. (1984) spectral atlas.

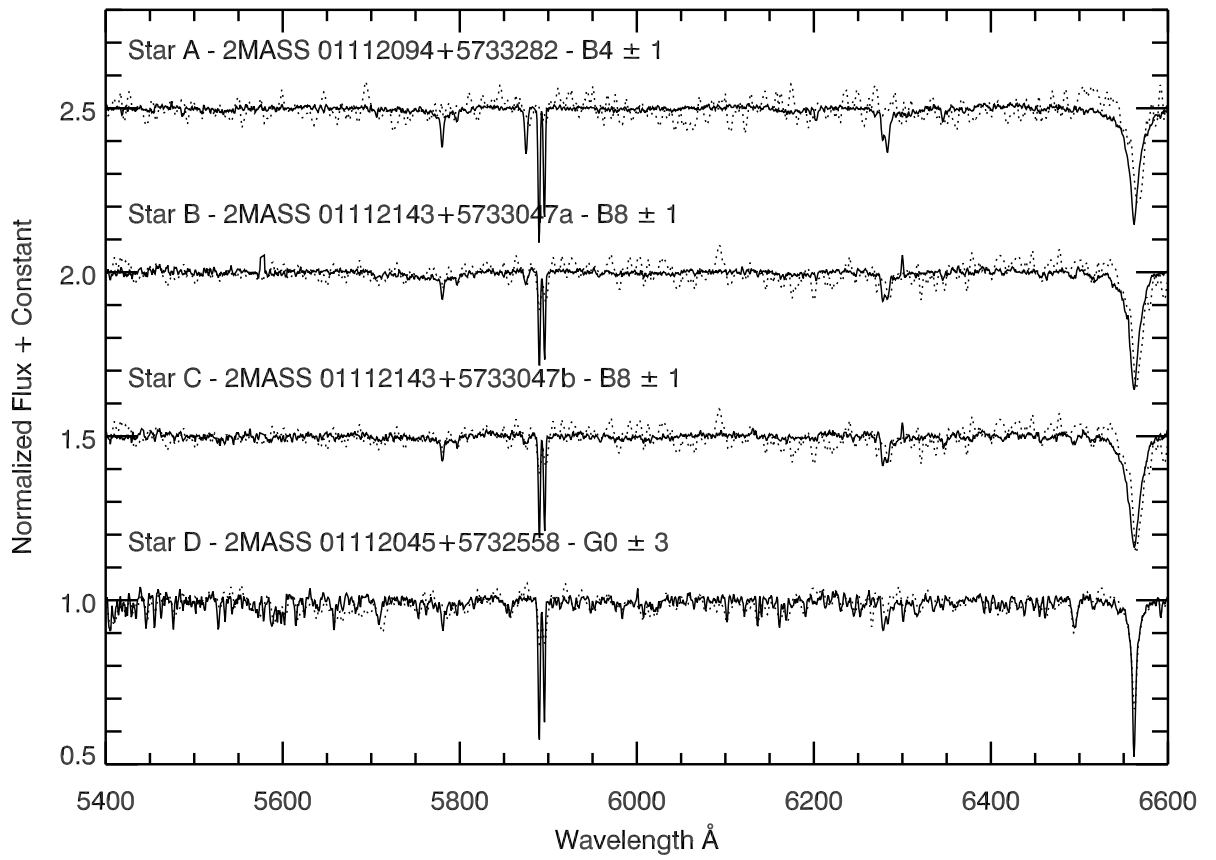


Fig. 12.— Continuum-normalized spectra (solid black lines) of the five stars selected for optical spectroscopy from IRAS01082+5717. The spectra are overplotted with red dotted lines of comparable spectral type from the Jacoby et al. (1984) spectral atlas.

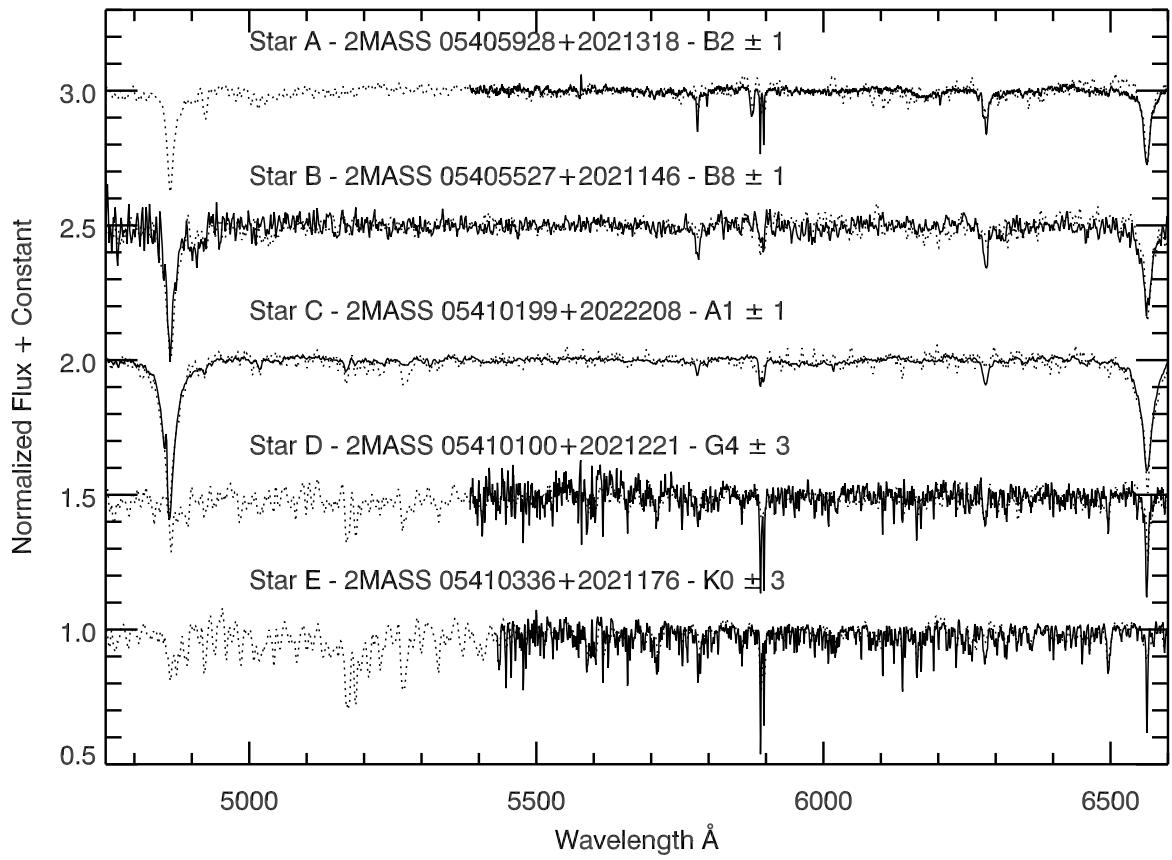


Fig. 13.— Continuum-normalized spectra (solid black lines) of the five stars selected for optical spectroscopy from IRAS05380+2020. The spectra are overplotted with red dotted lines of comparable spectral type from the Jacoby et al. (1984) spectral atlas.

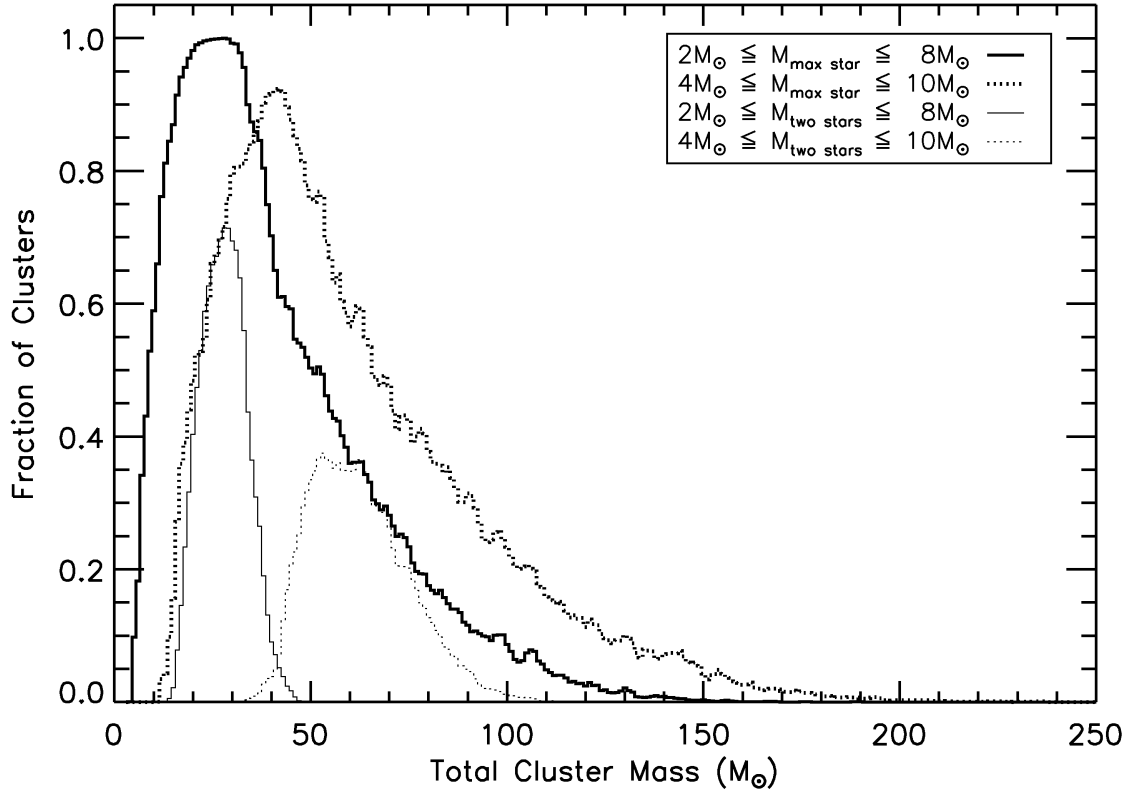


Fig. 14.— Fraction of simulated clusters in each total cluster mass bin that meet the specified stellar population criteria: the most massive star  $2M_{\odot} \leq M_{\text{max}} \leq 8M_{\odot}$  (solid bold line), the most massive star  $4M_{\odot} \leq M_{\text{max}} \leq 10M_{\odot}$  (dotted bold line), exactly two stars in the mass range  $2M_{\odot} \leq M \leq 8M_{\odot}$  including the most massive star (solid light line), and exactly two stars in the mass range  $4M_{\odot} \leq M \leq 10M_{\odot}$  including the most massive star (dotted light line).

Table 1. IM SFR Source Table

Number	<i>IRAS</i> Name	$\ell$ (°)	$b$ (°)	Morphological Classification
1	00001+6417	117.7266	2.1899	Blob/Shell
2	00002+6647	118.2070	4.6387	Filamentary
3	00025+6708	118.4940	4.9407	Blob/Shell
4	00034+6658	118.5597	4.7714	Filamentary
5	00063+6706	118.8581	4.8497	Filamentary
6	00070+6503	118.5951	2.8161	Blob/Shell
7	00080+6329	118.4449	1.2530	Blob/Shell
8	00127+6058	118.6205	-1.3256	Blob/Shell
9	00257+6601	120.6401	3.5368	Blob/Shell
10	00259+5625	119.8038	-6.0319	Blob/Shell
11	00265+6403	120.5441	1.5606	Blob/Shell
12	00268+6234	120.4521	0.0891	Blob/Shell
13	00278-3331	338.3160	-82.3784	Galaxy
14	00297-6431	306.4101	-52.7446	Galaxy
15	00299+6344	120.8924	1.2240	Blob/Shell
16	00307+6633	121.1843	4.0188	Blob/Shell
17	00331+6600	121.3862	3.4651	Star-like
18	00375+6637	121.8644	4.0443	Blob/Shell
19	00402+4120	121.2459	-21.2207	Blob/Shell
20	00420+5530	122.0145	-7.0718	Blob/Shell
21	00461-8104	303.1373	-36.3256	Galaxy
22	00487+5118	122.9572	-11.2944	Star-like
23	00497+6357	123.0781	1.3604	Blob/Shell
24	00555+7614	123.4011	13.6487	Galaxy
25	00571+6050	123.9965	-1.7503	Blob/Shell
26	00580+6238	124.0361	0.0595	Blob/Shell
27	00592+6413	124.1122	1.6434	Blob/Shell
28	01004+6031	124.4051	-2.0367	Blob/Shell
29	01036+5924	124.8675	-3.1395	Blob/Shell
30	01037+6504	124.5546	2.5255	Blob/Shell
31	01041+5828	124.9791	-4.0637	Blob/Shell
32	01056+6217	124.9340	-0.2501	Blob/Shell
33	01059+6222	124.9579	-0.1609	Blob/Shell
34	01082+5717	125.6137	-5.2090	Blob/Shell
35	01093+6523	125.1164	2.8669	Blob/Shell
36	01123+6430	125.5120	2.0293	Blob/Shell
37	01243+6212	127.1116	-0.1152	Blob/Shell
38	01312+6545	127.3270	3.5169	Blob/Shell
39	01431+6232	129.1969	0.5911	Blob/Shell
40	01467+5339	131.5807	-7.9748	Blob/Shell
41	01485-0957	164.6531	-67.6072	Galaxy
42	01485+2206	140.6824	-38.4415	Galaxy
43	01546+6319	130.2939	1.6549	Blob/Shell
44	01547+3540	137.6971	-25.0481	Galaxy
45	01565+1845	144.3888	-41.0192	Galaxy
46	01573+6730	129.4864	5.7738	Blob/Shell
47	01587+6148	131.1449	0.3118	Blob/Shell
48	02054+6011	132.3684	-1.0212	Blob/Shell
49	02071+3857	139.1875	-21.1834	Galaxy
50	02130+5509	134.8787	-5.5012	Blob/Shell
51	02149+6027	133.4125	-0.4020	Blob/Shell
52	02152+1418	152.3175	-43.3387	Galaxy
53	02160+6057	133.3721	0.1220	Blob/Shell
54	02207-2127	202.1398	-68.3194	Galaxy
55	02259+6044	134.5752	0.3272	Filamentary
56	02264+6034	134.6929	0.2044	Filamentary
57	02281-0309	171.6789	-56.1071	Galaxy
58	02309+6034	135.2053	0.4109	Blob/Shell
59	02312+2905	148.3953	-28.4284	Galaxy
60	02318+6106	135.0961	0.9404	Filamentary
61	02327+6019	135.5109	0.2576	Blob/Shell
62	02337+6029	135.5597	0.4672	Filamentary
63	02376+6030	135.9881	0.6722	Blob/Shell
64	02391+0013	171.3327	-51.7475	Galaxy
65	02398+2821	150.6756	-28.2308	Galaxy
66	02435-0747	182.4799	-56.5529	Galaxy
67	02436-5556	275.2021	-54.8324	Galaxy

Table 1—Continued

Number	<i>IRAS</i> Name	$\ell$ (°)	$b$ (°)	Morphological Classification
68	02438-0042	173.7439	-51.6511	Galaxy
69	02484+6022	137.2467	1.1153	Blob/Shell
70	02511+6023	137.5407	1.2788	Star-like
71	03050+5638	140.9113	-1.1620	Blob/Shell
72	03058+5941	139.4861	1.5326	Blob/Shell
73	03063+5735	140.5897	-0.2478	Blob/Shell
74	03083+5618	141.4780	-1.2309	Blob/Shell
75	03119+6017	139.8417	2.4399	Blob/Shell
76	03148+6011	140.2077	2.5398	Blob/Shell
77	03197-1534	202.1966	-53.1595	Galaxy
78	03208-3723	240.1602	-56.6872	Galaxy
79	03260-3719	239.8597	-55.6511	Galaxy
80	03298+5758	143.0278	1.7548	Blob/Shell
81	03300-5204	263.6453	-51.2017	Galaxy
82	03324+7224	134.7394	13.6326	Galaxy
83	03348-4407	250.9345	-52.9418	Galaxy
84	03353-2439	218.4592	-52.7067	Galaxy
85	03353+5550	144.8880	0.4516	Blob/Shell
86	03366+5536	145.1746	0.3758	Blob/Shell
87	03373-3129	229.7868	-53.3399	Galaxy
88	03387-2243	215.7328	-51.4541	Galaxy
89	03401-1338	202.8036	-47.8796	Galaxy
90	03404-4722	255.6891	-51.1964	Galaxy
91	03428-4448	251.5238	-51.3955	Galaxy
92	03478+5121	149.0845	-1.9839	Blob/Shell
93	03529+5345	148.1550	0.3718	Blob/Shell
94	03530+5117	149.7519	-1.5208	Blob/Shell
95	03544+5431	147.8406	1.0909	Blob/Shell
96	03571+5827	145.5748	4.3393	Blob/Shell
97	03583-8358	297.8124	-31.3864	Galaxy
98	04016+5508	148.2231	2.2366	Blob/Shell
99	04030+5000	151.7888	-1.4452	Blob/Shell
100	04030+5451	148.5615	2.1620	Blob/Shell
101	04128-6158	273.5884	-41.9946	Galaxy
102	04134-5611	266.1104	-43.8326	Galaxy
103	04155-6019	271.3592	-42.2641	Galaxy
104	04156+5251	151.2879	1.9669	Blob/Shell
105	04170-6253	274.5019	-41.1943	Galaxy
106	04170+7510	135.2231	17.7640	Galaxy
107	04189-5503	264.3086	-43.3912	Galaxy
108	04228+4653	156.3176	-1.4496	Blob/Shell
109	04235+4632	156.6519	-1.6130	Blob/Shell
110	04255+4829	155.4944	-0.0051	Blob/Shell
111	04275+3519	165.3121	-8.8075	Blob/Shell
112	04278+4417	158.7932	-2.6133	Blob/Shell
113	04418+4153	162.2995	-2.3383	Blob/Shell
114	04523+4718	159.3515	2.5707	Blob/Shell
115	04555-6632	277.2837	-36.1613	Filamentary
116	05000-7013	281.5112	-34.7879	Blob/Shell
117	05035-3802	241.6918	-36.4566	Galaxy
118	05068-7032	281.6952	-34.1539	Blob/Shell
119	05098-1544	216.6130	-28.9019	Galaxy
120	05129+3429	171.8899	-2.1318	Filamentary
121	05130+3420	172.0158	-2.2034	Filamentary
122	05132+3414	172.1283	-2.2184	Filamentary
123	05135+3657	169.9462	-0.5890	Blob/Shell
124	05142+3421	172.1595	-1.9855	Filamentary
125	05167+3858	168.6783	1.0891	Blob/Shell
126	05169-6722	277.7446	-33.9400	Blob/Shell
127	05183+3323	173.4276	-1.8585	Filamentary
128	05184+3635	170.8226	0.0034	Blob/Shell
129	05185+4002	167.9990	1.9890	Blob/Shell
130	05190-6928	280.1703	-33.3752	Blob/Shell
131	05197+3355	173.1612	-1.3037	Blob/Shell
132	05200+4221	166.2605	3.5513	Blob/Shell
133	05202-1132	213.4679	-24.8738	Galaxy
134	05212+3633	171.1705	0.4506	Blob/Shell

Table 1—Continued

Number	<i>IRAS</i> Name	$\ell$ (°)	$b$ (°)	Morphological Classification
135	05231+4121	167.4190	3.4557	Blob/Shell
136	05236+3828	169.8535	1.9217	Blob/Shell
137	05244+3829	169.9202	2.0534	Blob/Shell
138	05250-7134	282.5236	-32.4867	Star-like
139	05253+3504	172.8713	0.2910	Blob/Shell
140	05259-6952	280.5288	-32.7073	Blob/Shell
141	05266-7138	282.5708	-32.3493	Blob/Shell
142	05269+3728	171.0440	1.8999	Blob/Shell
143	05271-6909	279.6588	-32.7149	Star-like
144	05312-2158	225.2741	-26.5042	Galaxy
145	05313+3734	171.4401	2.6770	Blob/Shell
146	05319-0551	209.3107	-19.7774	Filamentary
147	05328+3650	172.2176	2.5291	Blob/Shell
148	05329+3628	172.5338	2.3505	Blob/Shell
149	05338-0529	209.2061	-19.1863	Filamentary
150	05339-6954	280.4384	-32.0225	Blob/Shell
151	05352-6933	280.0161	-31.9603	Blob/Shell
152	05363-0209	206.3951	-17.0866	Filamentary
153	05365-6627	276.3561	-32.1519	Filamentary
154	05365+6921	143.8245	19.4691	Galaxy
155	05378+2928	178.9940	-0.5414	Blob/Shell
156	05380+2020	186.7611	-5.3793	Blob/Shell
157	05382+3547	173.6984	2.8863	Blob/Shell
158	05394-0253	207.4466	-16.7588	Blob/Shell
159	05396+2855	179.6680	-0.5185	Blob/Shell
160	05404-0948	214.0728	-19.6516	Blob/Shell
161	05414+5840	153.9942	15.0129	Galaxy
162	05415-6419	273.8105	-31.7547	Galaxy
163	05416-7025	280.9437	-31.3133	Blob/Shell
164	05430-6913	279.5321	-31.3089	Filamentary
165	05445-1648	221.3092	-21.6508	Galaxy
166	05553+2642	183.3714	1.3164	Blob/Shell
167	05590-2340	229.5280	-21.1380	Galaxy
168	05591+2027	189.2145	-1.0633	Blob/Shell
169	05593+1711	192.0692	-2.6512	Blob/Shell
170	06008+3129	179.8076	4.7441	Blob/Shell
171	06045+3006	181.4117	4.7588	Blob/Shell
172	06052+8027	133.3600	25.2106	Galaxy
173	06056+1559	193.8578	-1.9366	Filamentary
174	06060+1655	193.0884	-1.4009	Blob/Shell
175	06061+2028	190.0086	0.3672	Blob/Shell
176	06065+2124	189.2287	0.8962	Blob/Shell
177	06070-6147	270.9708	-28.8169	Galaxy
178	06091+1510	194.9910	-1.5842	Blob/Shell
179	06110+1847	192.0311	0.5600	Blob/Shell
180	06133+2419	187.4357	3.6769	Blob/Shell
181	06145+1455	195.8206	-0.5676	Blob/Shell
182	06151+2246	188.9960	3.3023	Filamentary
183	06158+1506	195.8168	-0.2122	Blob/Shell
184	06164+0311	206.3954	-5.7395	Galaxy
185	06166+1724	193.8911	1.0527	Blob/Shell
186	06175+1108	199.5058	-1.7269	Blob/Shell
187	06178+1539	195.5535	0.4712	Blob/Shell
188	06181+1057	199.7220	-1.6925	Blob/Shell
189	06185-0828	217.1106	-10.6145	Galaxy
190	06201+2254	189.4303	4.3871	Blob/Shell
191	06212+1645	194.9733	1.7195	Blob/Shell
192	06220-8636	299.2014	-27.7463	Galaxy
193	06226+0733	203.2527	-2.3269	Blob/Shell
194	06279+0501	206.1139	-2.3251	Filamentary
195	06283+0516	205.9330	-2.1427	Filamentary
196	06293-0931	219.2729	-8.6864	Blob/Shell
197	06298+0444	206.5801	-2.0439	Filamentary
198	06299+0530	205.9171	-1.6867	Filamentary
199	06299+1011	201.7651	0.5067	Blob/Shell
200	06300+0530	205.9315	-1.6605	Filamentary
201	06314+0427	207.0233	-1.8335	Blob/Shell

Table 1—Continued

Number	<i>IRAS</i> Name	$\ell$ (°)	$b$ (°)	Morphological Classification
202	06315+0438	206.8671	-1.7282	Filamentary
203	06346+0600	206.0154	-0.4078	Blob/Shell
204	06348+0234	209.0797	-1.9494	Blob/Shell
205	06358+0047	210.7879	-2.5472	Blob/Shell
206	06375-0141	213.1883	-3.3297	Blob/Shell
207	06382+0939	203.2047	2.0796	Blob/Shell
208	06401-0318	214.9196	-3.4834	Blob/Shell
209	06416-0352	215.5998	-3.4146	Blob/Shell
210	06416+0701	205.9130	1.6078	Blob/Shell
211	06427+0507	207.7347	0.9616	Blob/Shell
212	06428-0257	214.9332	-2.7193	Blob/Shell
213	06428-2735	237.3049	-13.5519	Galaxy
214	06437-0703	218.6709	-4.4100	Blob/Shell
215	06446+0319	209.5591	0.5733	Blob/Shell
216	06448+0543	207.4402	1.7132	Blob/Shell
217	06454+0020	212.2855	-0.6185	Blob/Shell
218	06464-1650	227.7688	-8.2162	Star-like
219	06471-0353	216.2385	-2.1945	Blob/Shell
220	06486-0110	214.0149	-0.6110	Blob/Shell
221	06492-0349	216.4285	-1.7152	Blob/Shell
222	06495+0217	211.0385	1.1820	Blob/Shell
223	06507-0519	217.9316	-2.0697	Blob/Shell
224	06514-0424	217.1929	-1.4971	Blob/Shell
225	06520-0428	217.3210	-1.3716	Blob/Shell
226	06520+0018	213.0757	0.8215	Blob/Shell
227	06527-0027	213.8310	0.6186	Blob/Shell
228	06547-0806	220.8665	-2.4623	Blob/Shell
229	06552+1244	202.3403	7.1776	Galaxy
230	06559-0134	215.1948	0.8126	Blob/Shell
231	06571-0359	217.4910	-0.0236	Blob/Shell
232	06581-0848	221.8655	-2.0375	Blob/Shell
233	06581-0908	222.1599	-2.1827	Blob/Shell
234	06583-0346	217.4378	0.3387	Blob/Shell
235	06587-0859	222.0989	-1.9842	Blob/Shell
236	06592-1115	224.1811	-2.9162	Filamentary
237	07010-1143	224.7825	-2.7442	Filamentary
238	07011-0916	222.6324	-1.5956	Blob/Shell
239	07014-1141	224.8023	-2.6386	Filamentary
240	07029-1215	225.4778	-2.5741	Blob/Shell
241	07101+8550	127.6707	27.7055	Galaxy
242	07161-1311	227.8115	-0.1567	Filamentary
243	07173-1744	231.9603	-2.0588	Blob/Shell
244	07193-1727	231.9340	-1.5054	Blob/Shell
245	07195-1538	230.3515	-0.5991	Blob/Shell
246	07202-2209	236.1790	-3.5349	Blob/Shell
247	07208-1448	229.7719	0.0599	Blob/Shell
248	07216-2957	243.2396	-6.9192	Galaxy
249	07217-2933	242.8884	-6.7235	Galaxy
250	07221-2431	238.4804	-4.2797	Blob/Shell
251	07225-0933	225.3529	2.9403	Galaxy
252	07226-1602	231.0653	-0.1288	Blob/Shell
253	07260-2202	236.7134	-2.3092	Blob/Shell
254	07271-1937	234.7155	-0.9151	Blob/Shell
255	07272-1725	232.8013	0.1696	Blob/Shell
256	07273-1827	233.7254	-0.3198	Galaxy
257	07284-2203	236.9990	-1.8386	Blob/Shell
258	07288-6647	278.3912	-21.2502	Galaxy
259	07299-2432	239.3359	-2.7387	Blob/Shell
260	07301-1907	234.6278	-0.0593	Filamentary
261	07310-1444	230.8965	2.2661	Blob/Shell
262	07312-1444	230.9255	2.3182	Filamentary
263	07314-2306	238.2531	-1.7245	Blob/Shell
264	07333-2217	237.7469	-0.9585	Blob/Shell
265	07350-4731	260.2912	-12.6958	Galaxy
266	07395-2224	238.5598	0.2399	Galaxy
267	07429-2523	241.5383	-0.5937	Blob/Shell
268	07447+7428	140.4556	30.0433	Galaxy

Table 1—Continued

Number	<i>IRAS</i> Name	$\ell$ (°)	$b$ (°)	Morphological Classification
269	07455-2703	243.2626	-0.9398	Star-like
270	07466-2607	242.5847	-0.2401	Galaxy
271	07477-3343	249.2533	-3.9107	Blob/Shell
272	07492-2639	243.3415	-0.0086	Blob/Shell
273	07509-2614	243.1782	0.5233	Filamentary
274	07512-3406	249.9566	-3.4938	Blob/Shell
275	07527-2828	245.2993	-0.3023	Blob/Shell
276	07530-2513	242.5569	1.4470	Blob/Shell
277	07534-3618	252.0825	-4.2424	Blob/Shell
278	07538-3359	250.1341	-2.9643	Blob/Shell
279	07561-3304	249.5995	-2.0749	Blob/Shell
280	07568-4942	264.0143	-10.5777	Galaxy
281	07573-3035	247.6285	-0.5539	Blob/Shell
282	07583-4035	256.2484	-5.6478	Blob/Shell
283	07587-3050	248.0064	-0.4311	Blob/Shell
284	07598-2814	245.9268	1.1586	Blob/Shell
285	08041-2723	245.7097	2.4146	Galaxy
286	08044-3308	250.5938	-0.6453	Blob/Shell
287	08056-3513	252.4734	-1.5610	Blob/Shell
288	08076-2858	247.4649	2.1952	Blob/Shell
289	08129-3546	253.7495	-0.6305	Blob/Shell
290	08129-4547	262.0931	-6.2006	Blob/Shell
291	08130-3612	254.1238	-0.8663	Blob/Shell
292	08143-3521	253.5664	-0.1527	Filamentary
293	08150-2718	246.9794	4.4831	Galaxy
294	08158-3513	253.6270	0.1650	Blob/Shell
295	08163-3554	254.2472	-0.1369	Blob/Shell
296	08164-3819	256.2613	-1.4912	Blob/Shell
297	08165-4125	258.8333	-3.2252	Blob/Shell
298	08191-5009	266.3313	-7.7791	Blob/Shell
299	08206-4126	259.2753	-2.6122	Blob/Shell
300	08215-4030	258.6035	-1.9247	Blob/Shell
301	08236-4049	259.0948	-1.7835	Blob/Shell
302	08323-4247	261.6499	-1.6420	Blob/Shell
303	08327-4324	262.1771	-1.9604	Blob/Shell
304	08342-4150	261.0983	-0.7834	Blob/Shell
305	08346-4159	261.2611	-0.8131	Blob/Shell
306	08354-4754	266.0591	-4.3059	Blob/Shell
307	08360-5456	271.7749	-8.4565	Galaxy
308	08430-4751	266.8056	-3.2547	Blob/Shell
309	08435-4105	261.5795	1.0546	Filamentary
310	08445-4420	264.2264	-0.8455	Blob/Shell
311	08449-4449	264.6460	-1.1105	Blob/Shell
312	08460-4223	262.8880	0.5810	Filamentary
313	08476-4212	262.9293	0.9374	Filamentary
314	08485-2146	246.9606	13.8891	Galaxy
315	08486-4724	267.0551	-2.2493	Blob/Shell
316	08486-5231	271.0087	-5.5108	Blob/Shell
317	08500-4237	263.5311	1.0114	Blob/Shell
318	08509-4325	264.2508	0.6132	Blob/Shell
319	08533-4829	268.3854	-2.3428	Blob/Shell
320	08534-4231	263.8635	1.5482	Blob/Shell
321	08536-0222	230.8132	26.1078	Galaxy
322	08536-4917	269.0320	-2.8153	Blob/Shell
323	08586-3914	262.0206	4.4370	Galaxy
324	08597-4823	269.0018	-1.4733	Blob/Shell
325	09040-4924	270.2484	-1.6290	Blob/Shell
326	09070-7537	290.5253	-18.7190	Galaxy
327	09074-5056	271.7373	-2.2702	Blob/Shell
328	09080+7640	136.2554	34.3616	Galaxy
329	09086-4812	269.8674	-0.2616	Blob/Shell
330	09098-4725	269.4418	0.4229	Blob/Shell
331	09100-4922	270.8851	-0.8923	Blob/Shell
332	09121-5054	272.2124	-1.7048	Blob/Shell
333	09144-6251	281.1189	-9.7510	Galaxy
334	09147-4938	271.5911	-0.5282	Blob/Shell
335	09149-4756	270.4078	0.6797	Filamentary

Table 1—Continued

Number	<i>IRAS</i> Name	$\ell$ (°)	$b$ (°)	Morphological Classification
336	09162-4757	270.5742	0.8233	Blob/Shell
337	09165+7054	142.2633	37.5308	Galaxy
338	09166-4813	270.8197	0.6917	Blob/Shell
339	09216-5158	274.0236	-1.4056	Blob/Shell
340	09240-5431	276.0627	-2.9892	Blob/Shell
341	09248-5247	274.9432	-1.6565	Blob/Shell
342	09248-5403	275.8098	-2.5779	Blob/Shell
343	09274-5219	274.9051	-1.0512	Blob/Shell
344	09288-5427	276.5155	-2.4545	Blob/Shell
345	09293-5240	275.3651	-1.1048	Blob/Shell
346	09294-5336	276.0045	-1.7865	Blob/Shell
347	09394+0033	235.3712	37.2800	Galaxy
348	09409-5408	277.6288	-1.0533	Blob/Shell
349	09431+6809	143.9091	40.8936	Galaxy
350	09435-5130	276.2260	1.2166	Blob/Shell
351	09453-5647	279.8145	-2.6827	Blob/Shell
352	09459+7230	139.0136	38.6832	Galaxy
353	09496-7341	291.1485	-15.3595	Galaxy
354	09509-5513	279.4296	-0.9756	Blob/Shell
355	09514+6918	142.0908	40.9028	Galaxy
356	09570-5807	281.8701	-2.7516	Blob/Shell
357	09578-3118	265.2679	18.5123	Galaxy
358	09585+5555	157.8097	48.3597	Galaxy
359	09591-5710	281.5257	-1.8209	Blob/Shell
360	09595-5446	280.1324	0.1474	Blob/Shell
361	10011-5725	281.8836	-1.8522	Blob/Shell
362	10012-5825	282.4950	-2.6517	Blob/Shell
363	10015-0614	246.3780	37.3933	Galaxy
364	10020-5744	282.1787	-2.0363	Filamentary
365	10032-5756	282.4205	-2.1006	Blob/Shell
366	10056-5856	283.2633	-2.7285	Blob/Shell
367	10058-5718	282.3328	-1.3889	Blob/Shell
368	10092-5749	283.0031	-1.5565	Blob/Shell
369	10102-5706	282.7113	-0.8809	Blob/Shell
370	10111+0340	238.1556	45.5284	Galaxy
371	10116+0342	238.2030	45.6475	Galaxy
372	10124-2837	266.1190	22.5766	Galaxy
373	10126+7339	136.2914	39.4620	Galaxy
374	10142-5800	283.6499	-1.3283	Blob/Shell
375	10162-6037	285.3159	-3.3657	Blob/Shell
376	10195+2149	213.9642	55.7074	Galaxy
377	10213-5848	284.8780	-1.4955	Blob/Shell
378	10214-5928	285.2327	-2.0506	Blob/Shell
379	10245-5617	283.8979	0.8718	Blob/Shell
380	10271-5748	285.0023	-0.2429	Blob/Shell
381	10293-3941	275.8244	15.4424	Galaxy
382	10308-6122	287.2153	-3.0640	Blob/Shell
383	10311-5832	285.8253	-0.6061	Blob/Shell
384	10323-5729	285.4345	0.3888	Blob/Shell
385	10325-6023	286.9073	-2.1229	Filamentary
386	10335-5841	286.1697	-0.5856	Blob/Shell
387	10336-5725	285.5573	0.5304	Blob/Shell
388	10344-5947	286.8040	-1.4768	Blob/Shell
389	10457-5902	287.7203	-0.1422	Filamentary
390	10476-5953	288.3196	-0.7847	Filamentary
391	10516+5434	153.0552	55.4491	Galaxy
392	10531-5756	288.1084	1.2784	Blob/Shell
393	10533-5951	288.9452	-0.4411	Blob/Shell
394	10545-6050	289.5013	-1.2724	Blob/Shell
395	10556-6041	289.5617	-1.0847	Filamentary
396	10564-6252	290.5651	-3.0141	Filamentary
397	10580-5817	288.8315	1.2338	Blob/Shell
398	10589-5802	288.8378	1.5031	Blob/Shell
399	11017-6028	290.1548	-0.5780	Filamentary
400	11055-4615	284.9833	12.7027	Galaxy
401	11085-6158	291.4863	-1.6315	Blob/Shell
402	11109-5832	290.4952	1.6605	Blob/Shell

Table 1—Continued

Number	<i>IRAS</i> Name	$\ell$ (°)	$b$ (°)	Morphological Classification
403	11113+4835	158.1156	61.6335	Galaxy
404	11141-5938	291.2681	0.7937	Blob/Shell
405	11158-3232	281.2219	26.0974	Galaxy
406	11176+1315	241.9775	64.4194	Galaxy
407	11176+1351	240.8630	64.7835	Galaxy
408	11181+5326	149.5352	59.0365	Galaxy
409	11202+1651	235.5878	66.9681	Galaxy
410	11223-5840	291.9319	2.0623	Blob/Shell
411	11234+4351	163.6622	66.1933	Galaxy
412	11247+5709	143.8160	56.7176	Galaxy
413	11247+6651	135.2995	48.4789	Galaxy
414	11290-3001	283.1271	29.4726	Galaxy
415	11293-6250	294.0551	-1.6358	Blob/Shell
416	11294-6257	294.1055	-1.7419	Blob/Shell
417	11311-6335	294.4767	-2.2896	Filamentary
418	11313-6202	294.0293	-0.7924	Blob/Shell
419	11322-6108	293.8718	0.0894	Blob/Shell
420	11333-3743	286.8964	22.5121	Galaxy
421	11364-6254	294.8531	-1.4656	Filamentary
422	11383+1144	252.9422	67.2201	Galaxy
423	11398-6251	295.2003	-1.3030	Blob/Shell
424	11421-6223	295.3428	-0.7933	Blob/Shell
425	11423-6104	295.0275	0.4884	Blob/Shell
426	11427-6128	295.1776	0.1255	Blob/Shell
427	11434+4746	150.7196	65.9581	Galaxy
428	11436-5606	293.9312	5.3384	Galaxy
429	11442-6303	295.7370	-1.3770	Blob/Shell
430	11445-6237	295.6696	-0.9393	Blob/Shell
431	11449+5614	140.3019	58.9553	Galaxy
432	11457-6259	295.8871	-1.2729	Blob/Shell
433	11460+4859	148.1558	65.2273	Galaxy
434	11476-6435	296.4800	-2.7712	Blob/Shell
435	11478-6120	295.7333	0.3868	Blob/Shell
436	11510+4808	147.6353	66.4047	Galaxy
437	11514-2253	286.1394	37.8256	Galaxy
438	11535-1937	285.5865	41.1011	Galaxy
439	11556-6251	296.9612	-0.8894	Blob/Shell
440	11569-1859	286.3691	41.9299	Galaxy
441	11578-0049	277.3661	59.2144	Galaxy
442	11596+6224	132.7029	54.0480	Galaxy
443	12002+4854	143.3649	66.5181	Galaxy
444	12028+5037	140.5909	65.1640	Galaxy
445	12030+5049	140.3354	65.0097	Galaxy
446	12036+4951	141.1121	65.9165	Galaxy
447	12084-6258	298.4090	-0.7347	Blob/Shell
448	12085+5045	138.4714	65.4104	Galaxy
449	12085+6411	130.2453	52.6368	Galaxy
450	12102-6133	298.4088	0.6954	Blob/Shell
451	12138-4302	296.2108	19.0892	Galaxy
452	12145-5957	298.6977	2.3557	Blob/Shell
453	12162+1441	270.4315	75.1897	Galaxy
454	12171-6328	299.4579	-1.0951	Blob/Shell
455	12198-6213	299.6067	0.1752	Blob/Shell
456	12202-6222	299.6706	0.0365	Filamentary
457	12204+1605	271.1718	76.8989	Galaxy
458	12208-6242	299.7776	-0.2784	Blob/Shell
459	12235+1323	278.7856	74.7856	Galaxy
460	12239+3129	174.5443	83.1823	Galaxy
461	12294+1441	282.3436	76.5035	Galaxy
462	12295-6224	300.7477	0.1006	Blob/Shell
463	12315+0255	292.5934	65.1780	Galaxy
464	12340+1130	289.8096	73.7319	Galaxy
465	12362-6201	301.5071	0.5421	Blob/Shell
466	12378+6152	125.3257	55.4690	Galaxy
467	12380-0451	297.8897	57.6344	Galaxy
468	12396+3249	142.8293	84.2204	Galaxy
469	12412+1639	293.0776	79.1165	Galaxy

Table 1—Continued

Number	<i>IRAS</i> Name	$\ell$ (°)	$b$ (°)	Morphological Classification
470	12414+1324	295.4189	75.8908	Galaxy
471	12425-0011	299.5360	62.3677	Galaxy
472	12426-6512	302.3319	-2.6088	Blob/Shell
473	12436-6147	302.3632	0.7967	Blob/Shell
474	12469-6149	302.7530	0.7818	Blob/Shell
475	12481-6226	302.9036	0.1535	Blob/Shell
476	12482-6301	302.9182	-0.4271	Blob/Shell
477	12483+7308	123.0685	44.2527	Galaxy
478	12488-6214	302.9882	0.3519	Blob/Shell
479	12493+7154	122.9592	45.4933	Galaxy
480	12517-1015	304.1151	52.3296	Galaxy
481	12522+2912	101.5499	88.0524	Galaxy
482	12523+4648	121.2827	70.5867	Galaxy
483	12532+0434	305.7383	67.1529	Galaxy
484	12542+2157	315.7200	84.4209	Galaxy
485	12552-4559	304.1392	16.5903	Galaxy
486	12554+0150	306.7405	64.3981	Galaxy
487	12562-6228	303.8359	0.1052	Blob/Shell
488	12565-6257	303.8578	-0.3717	Blob/Shell
489	12575-6237	303.9784	-0.0420	Blob/Shell
490	12580+0246	308.4374	65.2742	Galaxy
491	12589-6113	304.1989	1.3533	Blob/Shell
492	13000-6258	304.2603	-0.3990	Blob/Shell
493	13023-6249	304.5208	-0.2604	Blob/Shell
494	13047-6321	304.7668	-0.8104	Blob/Shell
495	13086+3719	101.6115	79.2492	Galaxy
496	13099-1716	310.0721	45.0376	Galaxy
497	13100-6154	305.4721	0.5857	Filamentary
498	13111+3651	98.0453	79.4486	Galaxy
499	13135+4217	105.9986	74.2886	Galaxy
500	13137-6057	305.9954	1.5021	Filamentary
501	13142-1622	311.7203	45.8017	Galaxy
502	13149-3150	309.3858	30.4389	Galaxy
503	13158-6246	306.0657	-0.3295	Blob/Shell
504	13168-6246	306.1786	-0.3510	Blob/Shell
505	13170-2708	310.6333	35.0350	Galaxy
506	13225-4245	309.5121	19.4186	Galaxy
507	13231-6319	306.8226	-0.9748	Blob/Shell
508	13254-6125	307.3396	0.8647	Blob/Shell
509	13256-4839	309.2166	13.4991	Galaxy
510	13277+4727	104.8632	68.5583	Galaxy
511	13309-6241	307.7950	-0.4803	Blob/Shell
512	13350+0908	335.9316	68.7518	Galaxy
513	13353-1737	318.3161	43.5927	Galaxy
514	13357-6422	308.0336	-2.2352	Blob/Shell
515	13438-6203	309.3781	-0.1416	Blob/Shell
516	13445-6155	309.4917	-0.0184	Blob/Shell
517	13445-6200	309.4668	-0.1048	Blob/Shell
518	13470+3530	69.8649	75.2333	Galaxy
519	13543-6121	310.7509	0.2497	Blob/Shell
520	13549-3950	316.5027	21.0318	Blob/Shell
521	13558-6159	310.7633	-0.3946	Blob/Shell
522	14045+5057	96.8672	62.4427	Galaxy
523	14051-6147	311.8677	-0.5053	Star-like
524	14063-5930	312.6693	1.6281	Blob/Shell
525	14112-6034	312.9339	0.4348	Star-like
526	14131-6126	312.8766	-0.4614	Blob/Shell
527	14152-4309	319.2634	16.7065	Galaxy
528	14183-6036	313.7457	0.1154	Blob/Shell
529	14214+1451	7.4475	65.1372	Galaxy
530	14241-6007	314.5935	0.3265	Blob/Shell
531	14281-7809	308.1466	-16.5666	Galaxy
532	14283+3532	60.2793	67.3840	Galaxy
533	14284-5514	316.9109	4.6517	Galaxy
534	14290-6022	315.0666	-0.1288	Blob/Shell
535	14306+5808	100.0417	54.5068	Galaxy
536	14310+4940	88.6771	60.3860	Galaxy

Table 1—Continued

Number	<i>IRAS</i> Name	$\ell$ (°)	$b$ (°)	Morphological Classification
537	14326-6032	315.4111	-0.4537	Blob/Shell
538	14351+0230	353.1522	54.4551	Galaxy
539	14383-0006	351.2196	51.9773	Galaxy
540	14392-5916	316.6746	0.3652	Blob/Shell
541	14395-5941	316.5403	-0.0167	Blob/Shell
542	14500-5918	317.9014	-0.2476	Blob/Shell
543	14514+0344	359.4275	52.4204	Galaxy
544	14522-5932	318.0480	-0.5788	Filamentary
545	14526-5918	318.2051	-0.3977	Blob/Shell
546	14557-0053	355.3484	48.4324	Galaxy
547	14577-5748	319.4904	0.6190	Blob/Shell
548	15034-5839	319.7341	-0.4851	Blob/Shell
549	15035-6005	319.0333	-1.7413	Blob/Shell
550	15074-5744	320.6441	0.0469	Filamentary
551	15074-5909	319.9387	-1.1785	Blob/Shell
552	15077+5243	87.1590	53.9409	Galaxy
553	15082-5929	319.8548	-1.5157	Blob/Shell
554	15084+5711	93.2286	51.3984	Galaxy
555	15100-5903	320.2684	-1.2664	Blob/Shell
556	15103-5711	321.2671	0.3201	Blob/Shell
557	15106-2029	342.3464	31.1090	Galaxy
558	15109-5248	323.5948	4.0429	Galaxy
559	15115-6231	318.6322	-4.3265	Filamentary
560	15132+4223	69.6790	57.1670	Galaxy
561	15146+5629	91.5489	51.0874	Galaxy
562	15152-5601	322.4437	0.9603	Blob/Shell
563	15164-5650	322.1552	0.1839	Blob/Shell
564	15166-5706	322.0292	-0.0571	Blob/Shell
565	15174-5538	322.9054	1.1275	Blob/Shell
566	15229-5619	323.1814	0.1368	Blob/Shell
567	15249-5637	323.2421	-0.2682	Blob/Shell
568	15259-5612	323.6010	0.0005	Blob/Shell
569	15262-5541	323.9191	0.4010	Blob/Shell
570	15269-5632	323.5246	-0.3464	Blob/Shell
571	15342+1646	26.2496	50.4735	Galaxy
572	15347-5518	325.1268	0.0287	Blob/Shell
573	15360-5820	323.4827	-2.5284	Filamentary
574	15415-5337	326.9309	0.7841	Blob/Shell
575	15418-5449	326.2356	-0.2002	Filamentary
576	15472-5514	326.5836	-1.0010	Blob/Shell
577	15475-5239	328.2344	0.9986	Blob/Shell
578	15506-5325	328.1206	0.1044	Blob/Shell
579	15517-5334	328.1341	-0.1156	Star-like
580	15519-5430	327.5736	-0.8516	Blob/Shell
581	15522-5130	329.5179	1.4243	Blob/Shell
582	15583-5314	329.1075	-0.4881	Blob/Shell
583	16002-5533	327.7974	-2.4275	Star-like
584	16009-5130	330.5357	0.5508	Blob/Shell
585	16068-5116	331.3936	0.1135	Blob/Shell
586	16088-5012	332.3350	0.6827	Blob/Shell
587	16107-4956	332.7491	0.6726	Blob/Shell
588	16153-7001	319.0265	-14.1278	Galaxy
589	16162-5113	332.4872	-0.8576	Filamentary
590	16220-6304	324.5992	-9.7829	Galaxy
591	16228-2411	353.0489	17.0752	Filamentary
592	16254-4828	335.4802	0.0225	Blob/Shell
593	16266-4954	334.5905	-1.1005	Blob/Shell
594	16321-4755	336.6628	-0.4064	Filamentary
595	16345-4910	336.0107	-1.5436	Blob/Shell
596	16366-4746	337.2799	-0.8626	Blob/Shell
597	16404-4543	339.2350	0.0050	Blob/Shell
598	16409-4948	336.2183	-2.7395	Blob/Shell
599	16417-4445	340.1127	0.4780	Blob/Shell
600	16419-4602	339.1753	-0.3955	Blob/Shell
601	16440-4154	342.5519	2.0210	Blob/Shell
602	16448-4440	340.5467	0.1152	Blob/Shell
603	16459-4450	340.5329	-0.1478	Blob/Shell

Table 1—Continued

Number	<i>IRAS</i> Name	$\ell$ (°)	$b$ (°)	Morphological Classification
604	16486-4612	339.8008	-1.3907	Blob/Shell
605	16535-4300	342.8184	-0.0289	Blob/Shell
606	16544-4019	345.0188	1.5152	Filamentary
607	16562-4411	342.2135	-1.1537	Blob/Shell
608	16577+5900	88.0065	37.4306	Galaxy
609	17005-4152	344.5071	-0.3431	Blob/Shell
610	17023-3841	347.2419	1.3286	Blob/Shell
611	17026-4202	344.6225	-0.7532	Filamentary
612	17033-4035	345.8440	0.0255	Blob/Shell
613	17036-4134	345.0986	-0.6109	Blob/Shell
614	17039-3952	346.4879	0.3633	Star-like
615	17067-4518	342.4607	-3.3062	Blob/Shell
616	17073-4336	343.8894	-2.3809	Blob/Shell
617	17076-3858	347.6352	0.3400	Filamentary
618	17093-3604	350.1771	1.7915	Blob/Shell
619	17113-3620	350.1919	1.3059	Blob/Shell
620	17143-3400	352.4383	2.1790	Filamentary
621	17149-3404	352.4637	2.0258	Filamentary
622	17180+6039	89.6505	34.7005	Galaxy
623	17181-4405	344.6291	-4.2478	Blob/Shell
624	17191-3958	348.1259	-2.0442	Blob/Shell
625	17211-3537	351.9225	0.1099	Blob/Shell
626	17233-4012	348.3974	-2.8429	Blob/Shell
627	17285-3346	354.3082	-0.1077	Blob/Shell
628	17298-3253	355.1944	0.1362	Blob/Shell
629	17419-3207	357.2096	-1.5912	Blob/Shell
630	17468-3134	358.2208	-2.1904	Blob/Shell
631	17470-2533	3.3937	0.8832	Blob/Shell
632	17483-3114	358.6704	-2.2943	Blob/Shell
633	17499+7009	100.5727	30.6405	Galaxy
634	17518-2522	4.1071	0.0380	Star-like
635	17535-2431	5.0367	0.1392	Blob/Shell
636	17547-2555	3.9727	-0.7931	Blob/Shell
637	17567-2322	6.3984	0.0899	Star-like
638	17569+0617	32.6645	14.4178	Galaxy
639	17570-2310	6.6125	0.1415	Blob/Shell
640	17578+4553	72.8484	27.8555	Galaxy
641	18014-2428	5.9743	-1.3862	Star-like
642	18017-2207	8.0571	-0.2937	Filamentary
643	18024-2231	7.7918	-0.6330	Blob/Shell
644	18034-1359	15.3367	3.3801	Blob/Shell
645	18040-1503	14.4879	2.7253	Blob/Shell
646	18061-8525	308.0250	-26.4602	Galaxy
647	18081-2138	9.2061	-1.3495	Blob/Shell
648	18086-1846	11.7734	-0.0417	Blob/Shell
649	18106-1840	12.0879	-0.4133	Blob/Shell
650	18123-1203	18.0801	2.4181	Blob/Shell
651	18131-1606	14.6311	0.3007	Blob/Shell
652	18139-1704	13.8716	-0.3216	Star-like
653	18144-1700	13.9897	-0.4096	Star-like
654	18146-1200	18.4116	1.9387	Filamentary
655	18151-1134	18.8380	2.0399	Filamentary
656	18151-1318	17.3067	1.2182	Star-like
657	18163-1603	15.0345	-0.3530	Filamentary
658	18167-1614	14.9221	-0.5233	Star-like
659	18169-1338	17.2334	0.6804	Filamentary
660	18180-1342	17.3102	0.4007	Blob/Shell
661	18199-1603	15.4476	-1.1219	Blob/Shell
662	18210-1645	14.9612	-1.6875	Filamentary
663	18212+7432	105.5377	28.1747	Galaxy
664	18224-1228	18.8827	0.0520	Blob/Shell
665	18227-1218	19.0794	0.0612	Blob/Shell
666	18241-1320	18.3243	-0.7371	Blob/Shell
667	18253-1210	19.5033	-0.4438	Blob/Shell
668	18257-1226	19.3024	-0.6514	Star-like
669	18278+0111	31.6235	5.2451	Blob/Shell
670	18279-1039	21.1276	-0.2884	Blob/Shell

Table 1—Continued

Number	<i>IRAS</i> Name	$\ell$ (°)	$b$ (°)	Morphological Classification
671	18300-0458	26.3970	1.9036	Blob/Shell
672	18308-0741	24.0970	0.4533	Blob/Shell
673	18314-0517	26.2851	1.4493	Blob/Shell
674	18317-0926	22.6375	-0.5498	Filamentary
675	18318-0434	26.9737	1.6804	Blob/Shell
676	18318-0741	24.2007	0.2517	Blob/Shell
677	18322-0956	22.2576	-0.8800	Blob/Shell
678	18328-0900	23.1422	-0.5869	Star-like
679	18335+6705	97.2574	26.5584	Galaxy
680	18362-0517	26.8302	0.3822	Blob/Shell
681	18367-0529	26.7185	0.1741	Blob/Shell
682	18370-0607	26.1971	-0.1867	Blob/Shell
683	18411-0312	29.2414	0.2597	Blob/Shell
684	18412-0440	27.9651	-0.4425	Blob/Shell
685	18416-0518	27.4359	-0.8147	Star-like
686	18433-0327	29.2870	-0.3367	Blob/Shell
687	18441-0118	31.2780	0.4860	Star-like
688	18449+0032	33.0052	1.1520	Blob/Shell
689	18463-0052	31.9130	0.1963	Blob/Shell
690	18465-0018	32.4436	0.3973	Blob/Shell
691	18502-0018	32.8608	-0.4105	Blob/Shell
692	18504+0025	33.5378	-0.1291	Star-like
693	18527+0203	35.2640	0.1203	Blob/Shell
694	18530+0515	38.1304	1.5260	Blob/Shell
695	18537+0145	35.0979	-0.2412	Blob/Shell
696	18550+0358	37.2232	0.4788	Filamentary
697	18555+0910	41.9069	2.7739	Star-like
698	18559+0308	36.5844	-0.0961	Star-like
699	18564+0145	35.4139	-0.8500	Blob/Shell
700	18571+0326	36.9918	-0.2290	Blob/Shell
701	18582+0044	34.7313	-1.7170	Blob/Shell
702	18586+0106	35.0999	-1.6242	Blob/Shell
703	18588+0350	37.5475	-0.4082	Filamentary
704	19004+0119	35.5045	-1.9385	Star-like
705	19012+0505	38.9266	-0.3701	Blob/Shell
706	19014+0451	38.7527	-0.5245	Blob/Shell
707	19015+0212	36.4039	-1.7692	Blob/Shell
708	19015+0847	42.2405	1.2680	Blob/Shell
709	19023+0545	39.6476	-0.2926	Blob/Shell
710	19023+0601	39.8724	-0.1733	Blob/Shell
711	19027+0656	40.7432	0.1580	Blob/Shell
712	19040+0616	40.3061	-0.4308	Blob/Shell
713	19049+0712	41.2296	-0.1937	Blob/Shell
714	19056+0947	43.5996	0.8538	Blob/Shell
715	19060+0657	41.1443	-0.5620	Blob/Shell
716	19062+0531	39.8843	-1.2710	Blob/Shell
717	19062+0758	42.0522	-0.1198	Blob/Shell
718	19064+0539	40.0323	-1.2542	Blob/Shell
719	19071-5707	339.6960	-25.1342	Galaxy
720	19072+0649	41.1472	-0.8848	Blob/Shell
721	19079+0919	43.4512	0.1176	Blob/Shell
722	19100+1528	49.1330	2.5452	Blob/Shell
723	19105+0852	43.3515	-0.6641	Blob/Shell
724	19137+1013	44.9223	-0.7190	Blob/Shell
725	19138+1055	45.5381	-0.3986	Blob/Shell
726	19139+1045	45.4042	-0.5135	Blob/Shell
727	19150+1116	45.9857	-0.5046	Star-like
728	19152+1209	46.8000	-0.1284	Filamentary
729	19156+1441	49.0746	0.9810	Blob/Shell
730	19157+1319	47.8745	0.3110	Blob/Shell
731	19172+1558	50.3927	1.2426	Blob/Shell
732	19191+1733	51.9982	1.6064	Blob/Shell
733	19193+1443	49.5326	0.2092	Blob/Shell
734	19205+1447	49.7228	-0.0160	Blob/Shell
735	19207+1329	48.6018	-0.6683	Filamentary
736	19207+1348	48.8774	-0.5182	Blob/Shell
737	19208+6102	92.3093	20.0695	Galaxy

Table 1—Continued

Number	<i>IRAS</i> Name	$\ell$ (°)	$b$ (°)	Morphological Classification
738	19214+1556	50.8432	0.3349	Blob/Shell
739	19221+1456	50.0346	-0.2820	Blob/Shell
740	19230+1851	53.5789	1.3902	Blob/Shell
741	19233+1413	49.5402	-0.8814	Blob/Shell
742	19240+1907	53.9334	1.3222	Blob/Shell
743	19247+1829	53.4500	0.8710	Blob/Shell
744	19248+1730	52.6028	0.3740	Blob/Shell
745	19255+1531	50.9343	-0.7238	Blob/Shell
746	19256+1705	52.3339	0.0060	Blob/Shell
747	19260+1821	53.4841	0.5253	Blob/Shell
748	19266+1926	54.5134	0.9262	Blob/Shell
749	19273+1637	52.1156	-0.5759	Star-like
750	19295+1637	52.3691	-1.0479	Blob/Shell
751	19300+1852	54.3865	-0.0372	Blob/Shell
752	19315+2029	55.9763	0.4295	Blob/Shell
753	19330+1956	55.6672	-0.1300	Blob/Shell
754	19340+2336	58.9683	1.4616	Blob/Shell
755	19342+2235	58.1207	0.9133	Blob/Shell
756	19352+2717	62.3255	3.0202	Blob/Shell
757	19355+2055	56.8224	-0.1758	Blob/Shell
758	19359+2027	56.4486	-0.4811	Blob/Shell
759	19359+2746	62.8190	3.1445	Blob/Shell
760	19367+2152	57.7777	0.0488	Blob/Shell
761	19370+2601	61.4249	2.0612	Blob/Shell
762	19377+2229	58.4260	0.1590	Star-like
763	19389+2233	58.6294	-0.0336	Blob/Shell
764	19399-1026	29.3501	-16.0102	Galaxy
765	19405+2932	64.8605	3.1205	Blob/Shell
766	19415+2605	61.9719	1.2163	Blob/Shell
767	19422+2327	59.7854	-0.2489	Filamentary
768	19426+5559	88.6306	15.4485	Galaxy
769	19429+2320	59.7586	-0.4487	Blob/Shell
770	19433+2420	60.6730	-0.0171	Blob/Shell
771	19440+2344	60.2377	-0.4478	Blob/Shell
772	19455+2433	61.1136	-0.3362	Blob/Shell
773	19464+2641	63.0608	0.5738	Blob/Shell
774	19471+2532	62.1408	-0.1432	Blob/Shell
775	19478+2636	63.1358	0.2588	Blob/Shell
776	19480+2434	61.4188	-0.8319	Star-like
777	19494+2910	65.5202	1.2807	Blob/Shell
778	19497+3015	66.4949	1.7706	Blob/Shell
779	19523+2827	65.2471	0.3520	Blob/Shell
780	19542+3004	66.8394	0.8578	Blob/Shell
781	19544+2939	66.5024	0.6046	Filamentary
782	19560+3806	73.8889	4.7448	Filamentary
783	19566+2619	63.9243	-1.5682	Star-like
784	19578+3039	67.7505	0.4910	Blob/Shell
785	19597+3529	72.0483	2.7215	Blob/Shell
786	20001+3355	70.7723	1.8164	Blob/Shell
787	20022+3445	71.7041	1.9075	Filamentary
788	20028+2903	66.9629	-1.2804	Blob/Shell
789	20032+4249	78.6400	6.0584	Filamentary
790	20039+4101	77.1795	4.9811	Blob/Shell
791	20046+3139	69.3676	-0.2041	Blob/Shell
792	20053+3336	71.0915	0.7377	Blob/Shell
793	20056+3321	70.9064	0.5625	Blob/Shell
794	20060+3111	69.1425	-0.7010	Blob/Shell
795	20061+3431	71.9411	1.1055	Blob/Shell
796	20067+3520	72.6938	1.4389	Filamentary
797	20067+4405	80.0528	6.2017	Filamentary
798	20069+2819	66.8453	-2.4376	Blob/Shell
799	20077+4433	80.5522	6.2958	Filamentary
800	20080+3244	70.6612	-0.1976	Blob/Shell
801	20090+4231	78.9705	4.9951	Filamentary
802	20097+3250	70.9495	-0.4563	Filamentary
803	20097+4005	76.9887	3.5542	Blob/Shell
804	20098+4110	77.9041	4.1380	Filamentary

Table 1—Continued

Number	IRAS Name	$\ell$ (°)	$b$ (°)	Morphological Classification
805	20120+3949	77.0222	3.0447	Filamentary
806	20122+3936	76.8586	2.8779	Filamentary
807	20124+3601	73.9034	0.8623	Star-like
808	20125+4027	77.5946	3.3041	Filamentary
809	20129+4242	79.5122	4.5028	Filamentary
810	20134+3444	72.9526	-0.0254	Blob/Shell
811	20135+4138	78.6775	3.8151	Filamentary
812	20138+3632	74.4793	0.9115	Blob/Shell
813	20142+3552	73.9813	0.4749	Blob/Shell
814	20149+3440	73.0612	-0.3214	Blob/Shell
815	20149+3851	76.5300	2.0378	Filamentary
816	20151+3621	74.4769	0.5920	Blob/Shell
817	20152+3917	76.9230	2.2349	Filamentary
818	20152+3932	77.1201	2.3671	Filamentary
819	20153+3850	76.5478	1.9628	Blob/Shell
820	20154+3416	72.8095	-0.6339	Blob/Shell
821	20154+3937	77.2219	2.3871	Blob/Shell
822	20154+4202	79.2098	3.7518	Filamentary
823	20157+3854	76.6546	1.9253	Blob/Shell
824	20164+4042	78.2106	2.8417	Filamentary
825	20167+3903	76.8904	1.8595	Blob/Shell
826	20170+4609	82.8006	5.8245	Filamentary
827	20173+3714	75.4515	0.7318	Blob/Shell
828	20184+4054	78.5950	2.6458	Filamentary
829	20185+4119	78.9512	2.8667	Filamentary
830	20193+4356	81.2023	4.2308	Filamentary
831	20195+4504	82.1411	4.8535	Blob/Shell
832	20199+3731	75.9873	0.4686	Blob/Shell
833	20201+4311	80.6594	3.6839	Blob/Shell
834	20207+4206	79.8333	2.9796	Blob/Shell
835	20208+3908	77.4131	1.2560	Blob/Shell
836	20216+4319	80.9301	3.5345	Blob/Shell
837	20217+3947	78.0443	1.4915	Blob/Shell
838	20219+4256	80.6362	3.2676	Filamentary
839	20221-2458	18.8509	-30.8247	Galaxy
840	20222+3243	72.3323	-2.6805	Blob/Shell
841	20222+3541	74.7649	-0.9665	Blob/Shell
842	20223+4300	80.7381	3.2510	Filamentary
843	20228+3556	75.0305	-0.9190	Blob/Shell
844	20246+3658	76.0766	-0.6141	Filamentary
845	20252+4337	81.5401	3.1796	Filamentary
846	20257+3943	78.4459	0.8170	Filamentary
847	20260+4055	79.4422	1.4686	Filamentary
848	20261+3825	77.4396	-0.0055	Blob/Shell
849	20263+3748	76.9591	-0.3905	Blob/Shell
850	20272+3756	77.1707	-0.4659	Blob/Shell
851	20275+3842	77.8186	-0.0506	Filamentary
852	20282+3714	76.7169	-1.0451	Filamentary
853	20285+4250	81.2779	2.2312	Blob/Shell
854	20293+4007	79.1612	0.5033	Blob/Shell
855	20304+4059	79.9857	0.8408	Filamentary
856	20306+3958	79.1969	0.2156	Filamentary
857	20307+4015	79.4313	0.3640	Blob/Shell
858	20327+4120	80.5249	0.7151	Star-like
859	20337+4104	80.4388	0.4024	Filamentary
860	20338+3934	79.2545	-0.5220	Filamentary
861	20346+3911	79.0349	-0.8650	Filamentary
862	20357+4703	85.4086	3.7409	Blob/Shell
863	20358+3931	79.4436	-0.8634	Filamentary
864	20379+4020	80.3279	-0.6776	Filamentary
865	20384+3814	78.7377	-2.0378	Filamentary
866	20385+4022	80.4283	-0.7504	Filamentary
867	20409+4841	87.2431	4.0535	Blob/Shell
868	20422+4519	84.7449	1.7841	Blob/Shell
869	20452+3919	80.4101	-2.3957	Filamentary
870	20468+4559	85.7627	1.5773	Blob/Shell
871	20486-4857	350.6313	-39.6290	Galaxy

Table 1—Continued

Number	<i>IRAS</i> Name	$\ell$ (°)	$b$ (°)	Morphological Classification
872	20491+4855	88.2717	3.1390	Blob/Shell
873	20528+4903	88.7635	2.7698	Blob/Shell
874	20567+4821	88.6469	1.8248	Blob/Shell
875	21022+5205	92.0395	3.6448	Blob/Shell
876	21025+6801	104.2011	14.1134	Blob/Shell
877	21036+4854	89.8299	1.3461	Blob/Shell
878	21036+4903	89.9418	1.4451	Blob/Shell
879	21036+5107	91.4665	2.8283	Blob/Shell
880	21037+4933	90.3169	1.7703	Blob/Shell
881	21045+5252	92.8527	3.9104	Blob/Shell
882	21046+5110	91.6050	2.7439	Blob/Shell
883	21051+4950	90.6758	1.7812	Blob/Shell
884	21060+4937	90.6188	1.5439	Blob/Shell
885	21076+5322	93.5348	3.9024	Blob/Shell
886	21082+4804	89.7235	0.2110	Blob/Shell
887	21089-0214	48.6236	-31.7743	Galaxy
888	21093+4857	90.4906	0.6854	Blob/Shell
889	21108+5159	92.8610	2.6092	Filamentary
890	21112+5010	91.5961	1.3033	Star-like
891	21112+5232	93.3032	2.9281	Filamentary
892	21115+5203	92.9941	2.5713	Filamentary
893	21141+5133	92.8978	1.9346	Blob/Shell
894	21160+4810	90.7050	-0.6608	Blob/Shell
895	21163+5147	93.3043	1.8514	Filamentary
896	21169+5142	93.3168	1.7338	Blob/Shell
897	21181+5345	94.8981	3.0577	Blob/Shell
898	21188+5517	96.0514	4.0559	Blob/Shell
899	21191+5212	93.9064	1.8450	Blob/Shell
900	21223+4923	92.2943	-0.5171	Blob/Shell
901	21231+5002	92.8420	-0.1433	Blob/Shell
902	21248+5331	95.4437	2.1824	Blob/Shell
903	21260+4938	92.9033	-0.7472	Blob/Shell
904	21261+5413	96.0766	2.5627	Blob/Shell
905	21274+5111	94.1290	0.2142	Blob/Shell
906	21310+5651	98.3745	4.0150	Blob/Shell
907	21318-6407	329.3511	-41.8173	Galaxy
908	21355+5135	95.3336	-0.3410	Blob/Shell
909	21394+5128	95.7081	-0.8252	Blob/Shell
910	21410+5009	95.0495	-1.9891	Blob/Shell
911	21422+5249	96.9106	-0.0803	Blob/Shell
912	21422+5625	99.2355	2.6715	Blob/Shell
913	21450+5658	99.8882	2.8502	Filamentary
914	21466+7214	109.9984	14.4037	Galaxy
915	21481+5653	100.1659	2.5160	Blob/Shell
916	21482+5319	97.9281	-0.2608	Blob/Shell
917	21525+5539	99.8790	1.1709	Blob/Shell
918	21545+5736	101.2959	2.5310	Blob/Shell
919	21547+5855	102.1230	3.5645	Blob/Shell
920	21569+5923	102.6339	3.7585	Blob/Shell
921	22035+5435	100.4811	-0.6345	Blob/Shell
922	22052-5741	334.8229	-48.3678	Galaxy
923	22087+5520	101.5243	-0.4491	Blob/Shell
924	22112-6705	322.9952	-43.6887	Galaxy
925	22118-2742	23.1253	-55.3146	Galaxy
926	22147+5948	104.7120	2.7928	Blob/Shell
927	22148+6033	105.1348	3.4124	Blob/Shell
928	22151+5747	103.6371	1.0856	Blob/Shell
929	22160+5551	102.6639	-0.6052	Blob/Shell
930	22161+6140	105.8807	4.2454	Blob/Shell
931	22178+5607	103.0244	-0.5115	Blob/Shell
932	22181+5716	103.6858	0.4312	Blob/Shell
933	22224+5736	104.3533	0.4071	Blob/Shell
934	22282+6117	106.9036	3.1561	Blob/Shell
935	22350+5817	106.1434	0.1304	Blob/Shell
936	22374+6359	109.1731	4.9800	Star-like
937	22430+5832	107.1803	-0.1480	Blob/Shell
938	22451+5906	107.6837	0.2381	Blob/Shell

Table 1—Continued

Number	<i>IRAS</i> Name	$\ell$ ( $^{\circ}$ )	$b$ ( $^{\circ}$ )	Morphological Classification
939	22451+6154	108.9614	2.7211	Blob/Shell
940	22457+5751	107.1863	-0.9182	Blob/Shell
941	22460+6341	109.8690	4.2600	Blob/Shell
942	22488+5914	108.1712	0.1345	Blob/Shell
943	22507+6208	109.6597	2.6311	Filamentary
944	22519+5947	108.7588	0.4542	Blob/Shell
945	22546+5908	108.7978	-0.2751	Blob/Shell
946	22564+5849	108.8647	-0.6588	Blob/Shell
947	22575+1542	87.5666	-39.1224	Galaxy
948	22575+6158	110.3075	2.1432	Filamentary
949	22581+6352	111.1532	3.8421	Star-like
950	22587+6225	110.6203	2.4898	Filamentary
951	23004+5637	108.4471	-2.8913	Blob/Shell
952	23017+6007	110.0139	0.2579	Blob/Shell
953	23037+6213	111.0742	2.0859	Blob/Shell
954	23068+6117	111.0462	1.0846	Blob/Shell
955	23088+6014	110.8806	0.0156	Blob/Shell
956	23089+5914	110.5084	-0.9141	Blob/Shell
957	23107+5928	110.8112	-0.7919	Blob/Shell
958	23121+0415	82.8455	-50.6556	Galaxy
959	23131+5942	111.1817	-0.6811	Star-like
960	23146+5954	111.4219	-0.5604	Blob/Shell
961	23166-4231	348.0893	-65.9072	Galaxy
962	23179+2702	99.1958	-31.3253	Galaxy
963	23179+5804	111.1797	-2.4203	Blob/Shell
964	23192+5904	111.6787	-1.5503	Blob/Shell
965	23237+6351	113.7737	2.7899	Blob/Shell
966	23239+5826	112.0500	-2.3463	Blob/Shell
967	23260-4136	347.6851	-67.8769	Galaxy
968	23295+6016	113.2991	-0.8186	Blob/Shell
969	23347+6428	115.1042	3.0200	Blob/Shell
970	23384+6101	114.5590	-0.4189	Star-like
971	23435+5850	114.6073	-2.6867	Blob/Shell
972	23448+6010	115.1055	-1.4381	Blob/Shell
973	23464+6506	116.4742	3.3097	Blob/Shell
974	23498+6215	116.1731	0.4434	Blob/Shell
975	23504+6802	117.5447	6.0673	Blob/Shell
976	23506+6005	115.7847	-1.6884	Blob/Shell
977	23506+6224	116.2986	0.5760	Blob/Shell
978	23507+6230	116.3312	0.6603	Blob/Shell
979	23508+6807	117.6084	6.1416	Filamentary
980	23515+6016	115.9350	-1.5323	Blob/Shell
981	23528+6814	117.8075	6.2085	Filamentary
982	23568+6706	117.9515	5.0268	Filamentary
983	23586+6603	117.9151	3.9545	Blob/Shell
984	23593+6320	117.4610	1.2835	Blob/Shell

Table 2. Pilot Study IM SFRs

<i>IRAS</i> Name	$\ell$ (°)	$b$ (°)	$F_{12}$ (Jy)	$F_{25}$ (Jy)	$F_{60}$ (Jy)	$F_{100}$ (Jy)	Other ID
00259+5625	119.8038	-6.0319	0.7603	1.116	30.56	108.5	CB 3 <sup>a</sup> , LBN 594 <sup>b</sup>
00420+5530	122.0145	-7.0718	7.328	15.13	217.0	469.7	Mol 3 <sup>c</sup>
01082+5717	125.6137	-5.2090	1.138	1.089	13.56	44.78	—
05380+2020	186.7611	-5.3793	2.294	1.931	34.72	118.6	—

<sup>a</sup>(Clemens & Barvainis 1988)

<sup>b</sup>(Lynds 1965)

<sup>c</sup>(Molinari et al. 1996)

Table 3. Spectrophotometric Parameters

<i>IRAS</i> Name	2MASS ID	J	H	<i>K<sub>S</sub></i>	<i>H<math>\alpha</math></i> 6563		<i>He I</i> 5876		Sp. Type	<i>A<sub>V</sub></i> (mag)	<i>D<sub>spec</sub></i> (kpc)	<i>D<sub>lit</sub></i> (kpc)
(1)	(2)	(3)	(4)	(5)	EW	$\sigma$	EW	$\sigma$	(11)	(12)	(13)	(14)
00259+5625												2.5 <sup>a</sup> , 2.1 <sup>b</sup>
A	J00283934+5641507	13.089 <sup>c</sup>	12.896 <sup>c</sup>	12.737	8.00	0.57	0.30	0.13	B7	2.43 <sup>+0.07</sup> <sub>-0.09</sub>	2.12 <sup>+0.21+0.88</sup> <sub>-0.21</sub>	
B	J00284837+5641468	13.140	12.960	12.873	14.95	0.18	...	...	A1	1.03 <sup>+0.04</sup> <sub>-0.03</sub>	1.65 <sup>+0.04+0.68</sup> <sub>-0.06</sub>	
C	J00284282+5642554	12.958	12.632	12.590	4.53	0.20	...	...	F6	0.20 <sup>+0.03</sup> <sub>-0.04</sub>	0.91 <sup>+0.06+0.38</sup> <sub>-0.06</sub>	
D	J00284536+5641525	12.432	12.088	12.016	3.36	0.15	...	...	G0	0.50 <sup>+0.05</sup> <sub>-0.04</sub>	0.59 <sup>+0.05+0.25</sup> <sub>-0.05</sub>	
E	J00285071+5641430	11.226	10.512	10.285	1.44	0.21	...	...	G9	2.39 <sup>+0.05</sup> <sub>-0.41</sub>	0.19 <sup>+0.01+0.08</sup> <sub>-0.05</sub>	
00420+5530												5.0 <sup>d</sup> , 7.72 <sup>e</sup> , 2.17 <sup>f</sup>
A	J00444967+5546225	10.758	10.292	9.981	-8.66	0.02	0.19	0.02	B8e	...	...	
B	J00445732+5547231	11.288	10.598	10.183	4.49	0.27	0.73	0.12	B2	6.33 <sup>+0.17</sup> <sub>-0.17</sub>	1.14 <sup>+0.34+0.47</sup> <sub>-0.25</sub>	
C	J00450384+5546483 <sup>g</sup>	10.564	10.362	9.979	6.34	0.13	...	...	F2	4.75 <sup>+0.01</sup> <sub>-0.01</sub>	0.26 <sup>+0.01+0.11</sup> <sub>-0.01</sub>	
D	J00445393+5546244	10.826	12.620	12.489	4.00	0.07	...	...	F9	1.28 <sup>+0.05</sup> <sub>-0.04</sub>	0.71 <sup>+0.06+0.29</sup> <sub>-0.05</sub>	
01082+5717												...
A	J01112094+5733282	11.645	11.543	11.496	7.14	0.52	0.53	0.01	B4	1.22 <sup>+0.09</sup> <sub>-0.11</sub>	1.84 <sup>+0.26+0.76</sup> <sub>-0.23</sub>	
B	J01112143+5733047a <sup>h</sup>	11.499	11.412	11.279	7.40	0.06	0.15	0.02	B8	...	...	
C	J01112143+5733047b <sup>h</sup>	...	...	...	8.76	0.14	0.15	0.03	B8	...	...	
D	J01112045+5732558	12.453	12.099	11.990	3.80	0.07	...	...	G0	0.99 <sup>+0.05</sup> <sub>-0.04</sub>	0.57 <sup>+0.05+0.24</sup> <sub>-0.04</sub>	
05380+2020												...
A	J05405928+2021318	10.513	10.255	10.113	5.61	0.13	0.72	0.03	B2	2.74 <sup>+0.17</sup> <sub>-0.17</sub>	1.34 <sup>+0.40+0.55</sup> <sub>-0.30</sub>	
B	J05405527+2021146	12.018	11.684	11.529	6.63	0.20	0.19	0.06	B8	2.29 <sup>+0.09</sup> <sub>-0.22</sub>	1.10 <sup>+0.12+0.45</sup> <sub>-0.16</sub>	
C	J05410199+2022208	11.322	11.251	11.196	14.40	0.11	...	...	A1	0.61 <sup>+0.04</sup> <sub>-0.03</sub>	0.78 <sup>+0.02+0.32</sup> <sub>-0.04</sub>	
D	J05410100+2021221	13.188	12.674	...	2.94	0.24	...	...	G4	...	...	
E	J05410336+2021176	8.162	7.589	7.470	1.06	0.07	...	...	K0	0.80 <sup>+0.17</sup> <sub>-0.24</sub>	0.05 <sup>+0.01+0.02</sup> <sub>-0.01</sub>	

Note. — Spectrophotometric distances and *A<sub>V</sub>* include upper and lower limits resulting from the random uncertainty in spectral type and a second limit *upper-only* accounting for systematic uncertainty resulting from the unknown binarity status of each star

<sup>a</sup>Kinematic Distance (Launhardt & Henning 1997)

<sup>b</sup>Kinematic Distance (Yun & Clemens 1994)

<sup>c</sup>Upper Limit

<sup>d</sup>Kinematic Distance (Molinari et al. 2002)

<sup>e</sup>Kinematic Distance (Zhang et al. 2005)

<sup>f</sup>Maser Trigonometric Parallax (Moellenbrock et al. 2009)

<sup>g</sup>Foreground F star and background YSO both contributing flux

<sup>h</sup>Blended in 2MASS

Table 4. Candidate YSOs

<i>IRAS</i> Name	YSO ID	WISE ID	J	H	$K_S$	W1	W2	W3	W4
00259+5625	Y1	J002841.65+564152.7	17.111	14.439	12.371	10.460	9.262	6.667	3.736
	Y2	J002831.33+564419.9	11.998	11.770	11.656	11.410	11.281	7.827	5.799
	Y3	J002845.22+564307.6	17.233	14.718	12.744	11.271	10.181	8.412	6.298
	Y4	J002836.86+564245.4	16.267	14.490	13.672	12.564	11.858	7.134	4.341
00420+5530	Y5	J004356.01+555118.6	15.169	14.265	13.951	12.255	11.651	9.595	7.661
	Y6	J004503.67+554648.9	10.564	10.362	9.979	8.693	7.980	4.345	1.532
	Y7	J004414.63+554847.0	13.934	12.641	11.900	10.456	9.030	6.640	3.959
	Y8	J004412.68+554859.7	16.755	14.996	13.506	12.152	10.694	8.052	4.513
	Y9	J004409.63+554916.3	16.867	15.276	14.362	11.828	10.353	7.660	5.233
	Y10	J004421.45+554642.6	11.269	10.754	10.135	8.731	7.924	6.036	4.667
	Y11	J004413.27+555256.8	11.020	10.901	10.835	10.727	10.628	9.180	5.931
	Y12	J004457.31+554718.1	13.024	11.160	9.947	8.094	7.204	3.432	0.147
	Y13	J004412.78+555205.1	14.162	13.286	12.830	11.836	11.253	9.409	7.701
	Y14	J011122.88+573315.9	14.817	13.834	13.283	11.490	10.747	5.742	4.116
	Y15	J011121.12+573328.7	11.645	11.543	11.496	10.762	10.144	6.176	4.202
	Y16	J011111.23+573648.9	12.288	12.264	12.222	11.999	11.816	8.845	6.478
	Y17	J011123.14+573150.0	13.757	13.544	13.382	12.640	12.371	7.406	5.906
	Y18	J011134.42+573632.9	13.669	13.009	12.214	11.089	10.466	8.202	5.637
05380+2020	Y19	J054054.13+202247.7	16.930	16.224	15.180	10.255	9.325	6.580	3.967
	Y20	J054107.67+201806.9	15.775	14.932	14.502	13.873	13.092	8.897	5.182

Table 5. Candidate YSO Fitted Parameters

IRAS Name	ID	# of Fits	$\chi^2/n_{\text{data}}$	A <sub>V</sub>			M <sub>*</sub> (M <sub>⊕</sub> )		M <sub>*</sub> (M <sub>⊕</sub> )	$\log_{10}(M_{\text{disk}}/\text{M}_\odot)$	$\log_{10}(\dot{M}/\text{M}_\odot \text{yr}^{-1})$	$\log_{10}(L/\text{L}_\odot)$	Integer	Stage	F <sub>stage</sub>	$\sigma_{\text{stage}}$	
				BEST	BEST	AVG	BEST	AVG	Range	BEST	AVG	BEST	AVG	AVG	BEST	AVG	AVG
00259+5625																	
	Y1	294	0.03	24.72	24.09	3.7	4.0	1.5–5.7	-3.22	-1.41	-4.94	-4.37	2.14	I	amb	1.54	0.53
	Y2	163	0.94	0.00	0.42	2.3	2.8	0.8–3.7	-1.70	-2.55	-7.12	-6.32	1.39	II	II	2.07	0.19
	Y3	530	0.87	16.38	17.56	3.0	3.0	1.0–4.5	-1.31	-1.99	0.00	-6.26	1.82	II	II	1.99	0.02
	Y4	51	0.50	4.83	4.86	1.2	0.8	0.3–3.0	-1.62	-1.84	-4.91	-4.52	1.00	I	I	1.02	0.04
00420+5530																	
	Y5	41	2.73	5.63	5.18	1.9	1.9	0.1–2.8	-5.07	-2.95	0.00	-7.56	1.12	II	II	1.99	0.02
	Y6	24	0.87	2.27	2.44	5.2	5.1	4.8–5.2	-5.83	-5.54	0.00	0.00	2.70	III	amb	2.66	0.45
	Y7	33	1.18	0.46	0.66	1.3	2.6	0.1–4.6	-2.67	-1.12	-5.07	-4.39	1.44	I	I	1.06	0.11
	Y8	415	0.89	12.88	14.20	1.9	1.0	0.1–4.6	-2.32	-1.97	-5.55	-4.82	0.95	I	I	1.01	0.02
	Y9	30	2.18	12.64	12.06	3.0	2.1	0.2–3.8	-2.40	-2.06	0.00	-4.43	1.65	II	amb	1.63	0.46
	Y10	102	0.58	0.69	1.17	2.3	2.8	2.2–4.0	-2.13	-2.28	0.00	0.00	1.80	II	II	2.00	0.00
	Y11	55	0.88	1.76	1.08	2.3	2.5	2.0–2.7	-7.27	-5.80	0.00	-8.64	1.48	III	III	2.87	0.23
	Y12	174	0.21	3.69	3.10	6.8	5.3	0.9–7.4	-2.53	-1.25	-4.69	-4.33	2.41	I	I	1.01	0.01
	Y13	399	0.18	3.89	3.57	1.8	2.0	0.1–3.4	-4.38	-2.21	0.00	-7.54	1.17	II	II	2.01	0.06
01082+5717																	
	Y14	46	6.24	5.33	9.63	3.2	3.4	2.7–3.8	-4.45	-4.10	0.00	0.00	2.11	II	II	2.02	0.04
	Y15	16	3.49	0.03	1.12	3.2	3.1	3.0–3.2	-4.64	-3.33	0.00	0.00	1.77	II	II	2.00	0.00
	Y16	40	1.21	0.76	0.86	2.5	2.5	2.4–3.5	-5.36	-5.44	0.00	0.00	1.58	II	II	2.30	0.42
	Y17	11	5.85	2.31	2.79	2.2	2.3	2.3–2.5	-2.78	-2.89	0.00	0.00	1.48	II	II	2.00	0.00
	Y18	31	0.57	0.07	2.50	2.2	2.3	0.9–3.2	-2.17	-2.23	0.00	-8.23	1.37	II	II	2.00	0.00
05380+2020																	
	Y19	2	14.73	3.61	3.69	3.3	3.3	3.3–3.5	-3.07	-3.08	-3.21	-3.21	1.90	I	I	1.00	0.01
	Y20	25	0.62	4.58	3.60	1.3	1.0	0.1–3.2	-1.49	-1.65	-6.16	-4.96	0.84	II	amb	1.59	0.48